Z. Angew. Math. Phys. (2019) 70:44

https://doi.org/10.1007/s00033-019-1087-1

Zeitschrift für angewandte Mathematik und Physik ZAMP

Analysis of a linear 3D fluid–mesh–shell interaction problem

Sunčica Čanić, Marija Galić, Matko Ljulj, Boris Muha, Josip Tambača and Yifan Wang

Abstract. We study a linear fluid–structure interaction problem between an incompressible, viscous $3D$ fluid flow, a $2D$ linearly elastic Koiter shell, and an elastic $1D$ net of curved rods. This problem is motivated by studying fluid–structure interaction between blood flow through coronary arteries treated with metallic mesh-like devices called stents. The flow is assumed to be laminar, modeled by the time-dependent Stokes equations, and the structure displacement is assumed to be small, modeled by a system of linear Koiter shell equations allowing displacement in all three spatial directions. The fluid and the mesh-supported structure are coupled via the kinematic and dynamic coupling conditions describing continuity of velocity and balance of contact forces. The coupling conditions are evaluated along a linearized fluid–structure interface, which coincides with the fixed fluid domain boundary. No smallness on the structure velocity is assumed. We prove the existence of a weak solution to this linear fluid–composite structure interaction problem. This is the first result in the area of fluid–structure interaction that includes a $1D$ elastic mesh and takes into account structural displacements in all three spatial directions. Numerical simulations based on the finite element discretization of the coupled FSI problem are presented.

Mathematics Subject Classification. 74F10, 76D, 74K25, 35D30, 76M10.

1. Introduction

We study a fluid–structure interaction (FSI) problem between the flow of a viscous, incompressible fluid modeled by the time-dependent Stokes equations in a 3D cylindrical domain, and an elastic, composite structure, consisting of a cylindrical shell supported by a mesh-like elastic structure. A mesh-like structure is a 3D elastic body consisting of a collection of slender elastic rod-like components. The linear Koiter shell equations allowing displacement in all three spatial directions are used to model the elastodynamics of the lateral wall of the fluid domain cylinder, and a 1D hyperbolic net model consisting of a collection of linearly elastic curved rods is used to model the elastodynamics of the mesh-like structure. The mesh and the shell are coupled via the no-slip condition and via the balance of forces and moments. The resulting composite structure is then coupled to the fluid equations through the no-slip condition and balance of forces, which are evaluated at the *fixed* fluid–structure interface, giving rise to a linearly coupled FSI problem. This is a multiphysics fluid–structure interaction problem of mixed, parabolic–hyperbolic–hyperbolic type.

Problems of this type arise in many applications. In particular, the benchmark problem studied here was motivated by the interaction between the flow of blood in a coronary artery treated with a vascular device called a stent. In coronary arteries, the Reynolds number is small ($Re < 100$), thereby justifying the use of the time-dependent Stokes equations. Stents are metallic mesh-like devices used to prop the elastic coronary arteries open. The problem in this manuscript corresponds to FSI between blood flow and a fully expanded stent implanted in an elastic artery. A better understanding of the complex interactions between blood flow, artery and stent can lead to improved stent design (see, e.g., [11]).

Until recently, mathematical modeling of stents has been based almost exclusively on $3D$ approaches where a stent is assumed to be a single, $3D$ elastic body, approximated using $3D$-based finite elements. Such approaches are associated with large computer memory requirements and significant computing

Published online: 18 February 2019

time due to the slender nature of the local stent components, known as stent struts. To reduce computational costs, an alternative approach was suggested in [52], where a stent was modeled as a network of $1D$ curved rods, allowing the use of $1D$ finite elements for their numerical simulation. Although the model is one-dimensional, it provides $3D$ information about the deformation of stent struts in all three spatial directions. The resulting model has been justified both computationally [13] and mathematically [33,39,40].

In a recent work [12], this $1D$ stent net problem was coupled to an elastic shell of Naghdi type, and the corresponding *static* problem was analyzed. No fluid was considered in [12]. This contrasts the present work where *dynamic* models for both the stent and shell are considered, the shell is modeled using the cylindrical Koiter shell equations, and the resulting composite structure is coupled to the motion of an incompressible, viscous fluid.

In terms of the results related to the interaction between structures and incompressible, viscous fluids, we mention a few references which are most closely related to the present work in the area of analysis [16,17,19,24–26,29,32,38,44,45,47] and numerical simulations [4–6,9,10,27,37]. The fluid–structure interaction problems with composite structure were studied in [7,49]. The only works in which analysis of an FSI problem including an approximation of a stent-supported vessel were considered are [8,15]. In [15], a different, simplified, reduced coupled problems was studied, and in both papers the presence of a stent were modeled by the jump in the elasticity coefficients of a shell. In [8], a Koiter shell allowing only radial displacement was considered. This is significantly different from the present work where a stent is modeled as a separate mesh-like structure, and displacement in all three spatial directions is taken into account. In fact, one of the goals of our future research is to compare the results of the present manuscript with those of [8] to understand the impact of the full coupling between the stent and shell on the elastodynamics of the composite structure.

In the present manuscript, we prove the existence of a weak solution to the coupled fluid–mesh–shell interaction problem by adapting the methodology introduced in [47] (see also [36]) where the existence of a weak solution to a nonlinear moving boundary FSI problem involving a $2D$ incompressible Newtonian fluid and a $1D$ linearly elastic shell was proved. The method is based on a semi-discretization approach, where the coupled problem is discretized in time, and at the same time split into a fluid and a structure subproblem using the so-called Lie operator splitting strategy (for more information about splitting methods see, e.g., [30,31]). The main feature of this method is that it allows decoupling the problem into subproblems with different physics, and is, therefore, especially suitable for complex multiphysics problems [7,46,48–51]. The constructed weak solutions are of Leray type, and they satisfy an energy inequality. Based on a carefully designed splitting strategy, uniform energy estimates can be obtained, and existence of weak and weak*-convergent subsequences established. We note that the regularity in space for the 1D hyperbolic net displacement considered in this work, is obtained from the inextensibility and unshearability condition of curved rods, and not directly from the energy estimates. The resulting regularity provides sufficient information to pass to the limit in the weak formulation of the semi-discrete problem. Because the problem we consider is linear, limits of the weakly and weakly*-convergent subsequences can be shown to satisfy the weak formulation of the coupled continuous FSI problem.

Although the displacement of the composite structure is considered small, the velocity of displacement is not necessarily small and is taken into account in the coupling conditions at the interface. Due to the smallness of displacement, the fluid–structure interface is considered to be fixed (linearized). Such, somewhat restrictive, assumption has been used frequently in FSI problems (see, e.g., [2,3,14,18,26,43] and the references therein). The extension of our analysis to the nonlinear case involving moving boundaries is challenging and will be addressed in our future work.

In summary, the main novelties of the present work are:

1. Analysis of an *evolution* problem for a mesh-like structure, modeled as a $1D$ hyperbolic net.
2. A fluid–mesh–shell interaction model that takes into account the structure displacement in *all three directions*.
3. An *existence result* for the coupled fluid–mesh–shell linear problem.

4. A *constructive* proof giving rise to a loosely coupled partitioned scheme for the fluid–mesh–shell interaction problem.

Details of the result are presented in the following six sections, with the last section ("Appendix") dedicated to the summary of notation used in the paper to help the reader get through the details of the proof. Theoretical results are illustrated by numerical examples in Sect. 8.

2. Model description

2.1. The fluid

We consider the flow of an incompressible, viscous fluid through a cylindrical domain, denoted by Ω:

$$\Omega = \{(z, x, y) \in \mathbb{R}^3 : z \in (0, L), \sqrt{x^2 + y^2} \leq R\}.$$

The fluid domain boundary consists of three parts: the lateral boundary Γ, which is a cylinder of radius R, the inlet boundary Γ_{in}, which is a circular area of radius R located at $z = 0$, and the outlet boundary Γ_{out}, which is a circular area of radius R, located at $z = L$.

The time-dependent Stokes equations for an incompressible, viscous fluid are used to model the flow in Ω:

$$\left.\begin{array}{c} \rho_F \partial_t \mathbf{u} = \nabla \cdot \boldsymbol{\sigma} \\ \nabla \cdot \mathbf{u} = 0 \end{array}\right\} \text{ in } \Omega, \quad t \in (0, T), \tag{1}$$

where ρ_F denotes the fluid density, $\mathbf{u}$ is the fluid velocity, $\boldsymbol{\sigma} = -pI + 2\mu_F \mathbf{D}(\mathbf{u})$ is the fluid Cauchy stress tensor, p is the fluid pressure, μ_F is the dynamic viscosity coefficient, and $\mathbf{D}(\mathbf{u}) = \frac{1}{2}(\nabla \mathbf{u} + \nabla^T \mathbf{u})$ is the symmetrized gradient of $\mathbf{u}$. At the inlet and outlet, we prescribe the pressure, with the tangential fluid velocity equal to zero (see [23]):

$$\left.\begin{array}{c} p = P_{\text{in/out}}(t) \\ \mathbf{u} \times \mathbf{e}_z = 0 \end{array}\right\} \text{ on } \Gamma_{\text{in/out}},$$

where $P_{\text{in/out}}$ are given. Therefore, the fluid flow is driven by the pressure drop, and the fluid flow is orthogonal to the inlet and outlet boundary.

The fluid velocity will be assumed to belong to the following classical function space

$$V_F = \{\mathbf{u} \in H^1(\Omega; \mathbb{R}^3) : \nabla \cdot \mathbf{u} = 0, \mathbf{u} \times \mathbf{e}_z = 0 \text{ on } \Gamma_{\text{in/out}}\}. \tag{2}$$

2.2. The shell

The lateral boundary of the fluid domain will be assumed elastic, and modeled by the cylindrical Koiter shell equations. The shell thickness will be denoted by $h > 0$, the length by L, and its reference radius of the middle surface by R. We consider a clamped cylindrical shell. This reference configuration, which we denote by Γ, can be parameterized by

$$\boldsymbol{\varphi} : \omega \to \mathbb{R}^3, \quad \boldsymbol{\varphi}(z, \theta) = (R\cos\theta, R\sin\theta, z),$$

where $\omega = (0, L) \times (0, 2\pi)$, and $R > 0$, thus:

$$\Gamma = \{(R\cos\theta, R\sin\theta, z) : z \in (0, L), \theta \in (0, 2\pi)\}.$$

The first fundamental form of the cylinder Γ, also known as the metric tensor, will be denoted by A_{c} in covariant components, and by A_{c} in contravariant components:

$$A_{\text{c}} = \begin{pmatrix} 1 & 0 \\ 0 & R^2 \end{pmatrix}, \quad A^c = \begin{pmatrix} 1 & 0 \\ 0 & \frac{1}{R^2} \end{pmatrix},$$

and the area element is $\mathrm{d}S = \sqrt{\det A_c}\ \mathrm{d}z\mathrm{d}\theta = R\ \mathrm{d}z\mathrm{d}\theta$. The second fundamental form of the cylinder Γ or the curvature tensor in covariant components is given by

$$B_c = \begin{pmatrix} 0 & 0 \\ 0 & R \end{pmatrix}.$$

Under loading, the Koiter shell is displaced from its reference configuration Γ by a displacement $\boldsymbol{\eta} = \boldsymbol{\eta}(t,z,\theta) = (\eta_z, \eta_r, \eta_\theta)$, where η_z, η_r, and η_θ denote the tangential, radial and azimuthal components of displacement. The end points of the shell will be assumed to be clamped, giving rise to the following boundary conditions:

$$\begin{aligned} \boldsymbol{\eta}(t,0,\theta) = \boldsymbol{\eta}(t,L,\theta) = 0, \quad \theta \in (0,2\pi), \\ \partial_z \eta_r(t,0,\theta) = \partial_z \eta_r(t,L,\theta) = 0, \quad \theta \in (0,2\pi), \end{aligned}$$

whereas the boundary conditions at $\theta = 0, 2\pi$, will be periodic:

$$\begin{aligned} \boldsymbol{\eta}(t,z,0) = \boldsymbol{\eta}(t,z,2\pi), \quad z \in (0,L), \\ \partial_\theta \eta_r(t,z,0) = \partial_\theta \eta_r(t,z,2\pi), \quad z \in (0,L). \end{aligned}$$

The elastic properties of the shell are defined by the following elasticity tensor $\mathcal{A}$:

$$\mathcal{A}E = \frac{2\lambda\mu}{\lambda + 2\mu}(A^c \cdot E)A^c + 2\mu A^c E A^c, \quad E \in \mathrm{Sym}(\mathbb{R}^2),$$

where λ and μ are Lamé constants. Tensor $\mathcal{A}$ defines the following elastic energy of the deformed Koiter shell:

$$E(\boldsymbol{\eta}) = \frac{h}{2}\int_\omega \mathcal{A}\boldsymbol{\gamma}(\boldsymbol{\eta}) : \boldsymbol{\gamma}(\boldsymbol{\eta}) R + \frac{h^3}{24}\int_\omega \mathcal{A}\boldsymbol{\varrho}(\boldsymbol{\eta}) : \boldsymbol{\varrho}(\boldsymbol{\eta}) R, \tag{3}$$

where $\boldsymbol{\gamma}$ denotes the linearized change of metric tensor, measuring the stretch of the middle surface (membrane effects), and $\boldsymbol{\varrho}$ denotes the linearized change of curvature tensor, measuring flexure (bending, shell effects). They are given by:

$$\boldsymbol{\gamma}(\boldsymbol{\eta}) = \begin{pmatrix} \partial_z \eta_z & \frac{1}{2}(\partial_\theta \eta_z + R\partial_z \eta_\theta) \\ \frac{1}{2}(\partial_\theta \eta_z + R\partial_z \eta_\theta) & R\partial_\theta \eta_\theta + R\eta_r \end{pmatrix},$$

$$\boldsymbol{\varrho}(\boldsymbol{\eta}) = \begin{pmatrix} -\partial_{zz}\eta_r & -\partial_{z\theta}\eta_r + \partial_z \eta_\theta \\ -\partial_{z\theta}\eta_r + \partial_z \eta_\theta & -\partial_{\theta\theta}\eta_r + 2\partial_\theta \eta_\theta + \eta_r \end{pmatrix}.$$

Let V_K denote the following function space:

$$\begin{aligned} V_K = \{ &\boldsymbol{\eta} = (\eta_z, \eta_r, \eta_\theta) \in H^1(\omega) \times H^2(\omega) \times H^1(\omega) : \\ &\boldsymbol{\eta}(t,z,\theta) = \partial_z \eta_r(t,z,\theta) = 0, z \in \{0, L\}, \theta \in (0,2\pi), \\ &\boldsymbol{\eta}(t,z,0) = \boldsymbol{\eta}(t,z,2\pi), \partial_\theta \eta_r(t,z,0) = \partial_\theta \eta_r(t,z,2\pi), z \in (0,L)\}, \end{aligned} \tag{4}$$

equipped with the corresponding norm:

$$\|\boldsymbol{\eta}\|_k^2 = \|\eta_z\|_{H^1(\omega)}^2 + \|\eta_r\|_{H^2(\omega)}^2 + \|\eta_\theta\|_{H^1(\omega)}^2.$$

We are interested in weak solutions $\boldsymbol{\eta} = (\eta_z, \eta_r, \eta_\theta) \in V_K$ satisfying the following elastodynamics problem for a cylindrical Koiter shell (see [22,41,42]): find $\boldsymbol{\eta} = (\eta_z, \eta_r, \eta_\theta) \in V_K$ such that

$$\rho_K h \int_\omega \partial_t^2 \boldsymbol{\eta} \cdot \boldsymbol{\psi} R + \langle \mathcal{L}\boldsymbol{\eta}, \boldsymbol{\psi} \rangle = \int_\omega \mathbf{f} \cdot \boldsymbol{\psi} R, \quad \forall \boldsymbol{\psi} \in V_K, \tag{5}$$

where ρ_K is the shell density, $\mathbf{f}$ is the outside loading, and $\mathcal{L}$ is the linear operator associated with the Koiter elastic energy (3):

$$\langle \mathcal{L}\boldsymbol{\eta}, \boldsymbol{\psi} \rangle = h \int_\omega \mathcal{A}\boldsymbol{\gamma}(\boldsymbol{\eta}) : \boldsymbol{\gamma}(\boldsymbol{\psi}) R + \frac{h^3}{12} \int_\omega \mathcal{A}\boldsymbol{\varrho}(\boldsymbol{\eta}) : \boldsymbol{\varrho}(\boldsymbol{\psi}) R.$$

We emphasize that from Theorems 2.6 to 4 in [21], we get the coercivity of the operator $\mathcal{L}$, i.e., $\langle \mathcal{L}\boldsymbol{\eta}, \boldsymbol{\eta} \rangle \geq c\|\boldsymbol{\eta}\|_k^2$, $\forall \boldsymbol{\eta} \in V_K$. The differential form of the cylindrical Koiter shell elastodynamics problem on $(0,T)\times\omega$ is then given by:

$$\rho_K h \partial_t^2 \boldsymbol{\eta} R + \mathcal{L}\boldsymbol{\eta} = \mathbf{f} R, \tag{6}$$

where $\mathbf{f}$ is outside force density, and $\mathcal{L}$ corresponds to the elastic force associated with the elastic energy (3).

2.3. The elastic mesh

An elastic mesh is a three-dimensional elastic body defined as a union of three-dimensional slender components called struts [13,52]. Since struts are slender or "thin", meaning that the ratio between the thickness of each strut versus its length is small, 1D (reduced) models can be used to approximate their elastodynamic properties. In particular, keeping the stent application in mind, we will be using a 1D curved rod model to approximate the elastodynamic properties of slender mesh struts. The one space dimension corresponds to the parameterization of the middle line of curved rod. For the i-th curved rod, the middle line is parameterized via

$$\mathbf{P}_i : [0, l_i] \to \boldsymbol{\varphi}(\overline{\omega}), \quad i = 1, \ldots, n_E,$$

where n_E denotes the number of curved rods in a mesh. By using $s \in (0, l_i)$ to denote the location along the middle line, and $\mathbf{d}_i(t,s)$ to denote the displacement of the middle line from its reference configuration, $\mathbf{w}_i(t,s)$ the infinitesimal rotation of cross sections, $\mathbf{q}_i(t,s)$ the contact moment, and $\mathbf{p}_i(t,s)$ the contact force, the following system of equations will be used to model the elastodynamics of 1D curved rods:

$$\begin{aligned} \rho_S A_i \partial_t^2 \mathbf{d}_i &= \partial_s \mathbf{p}_i + \mathbf{f}_i, \\ \rho_S M_i \partial_t^2 \mathbf{w}_i &= \partial_s \mathbf{q}_i + \mathbf{t}_i \times \mathbf{p}_i, \\ 0 &= \partial_s \mathbf{w}_i - Q_i H_i^{-1} Q_i^T \mathbf{q}_i, \\ 0 &= \partial_s \mathbf{d}_i + \mathbf{t}_i \times \mathbf{w}_i. \end{aligned} \tag{7}$$

Here, ρ_S is the strut's material density, A_i is the cross-sectional area of the i-th rod, M_i is the matrix related to the moments of inertia of the cross sections, $\mathbf{f}_i$ is the line force density acting on the i-th rod, and $\mathbf{t}_i$ is the unit tangent on the middle line of the i-th rod. Matrix H_i is a positive definite matrix which describes the elastic properties and the geometry of the cross section, while matrix $Q_i \in SO(3)$ represents the local basis at each point of the middle line of the i-th rod (see [1] for more details). The first two equations describe the linear impulse-momentum law and the angular impulse-momentum law, respectively, while the last two equations describe a constitutive relation for a curved, linearly elastic rod, and the condition of inextensibility and unshearability, respectively.

System (7) is defined on a graph domain, determined by the geometry and topology of the mesh structure. The graph consists of a set of vertices $\mathcal{V}$ (points where the middle lines meet), and a set of edges $\mathcal{E}$ (pairing of vertices). The ordered pair $\mathcal{N} = (\mathcal{V}, \mathcal{E})$ defines the mesh net topology. At each vertex $V \in \mathcal{V}$, the following coupling conditions are enforced:

- Kinematic coupling conditions describing continuity of displacements and infinitesimal rotations,
- Dynamic coupling conditions describing the balance of contact forces and contact moments.

Here, we note that even though each individual stent strut is inextensible, the struts can deform (bend) to accommodate the overall expansion or contraction of the stent radius, which influences the overall length of the stent. The impact of inextensibility of stent struts will be discussed in Sect. 8.

We are interested in weak solutions to the 1D mesh net problem, i.e., to the problem consisting of all the functions satisfying the system of linear equations (7) on a graph domain, with the above-mentioned coupling conditions holding at graph's vertices. To define the weak solution space, we first introduce a function space consisting of all the H^1-functions $(\mathbf{d}, \mathbf{w})$ defined on the entire net $\mathcal{N}$, such that they satisfy the kinematic coupling conditions at each vertex $V \in \mathcal{V}$:

$$H^1(\mathcal{N};\mathbb{R}^6) = \{(\mathbf{d},\mathbf{w}) = ((\mathbf{d}_1,\mathbf{w}_1),\ldots,(\mathbf{d}_{n_E},\mathbf{w}_{n_E})) \in \prod_{i=1}^{n_E} H^1(0,l_i;\mathbb{R}^6) : \\ \mathbf{d}_i(\mathbf{P}_i^{-1}(V)) = \mathbf{d}_j(\mathbf{P}_j^{-1}(V)), \mathbf{w}_i(\mathbf{P}_i^{-1}(V)) = \mathbf{w}_j(\mathbf{P}_j^{-1}(V)), \\ \forall V \in \mathcal{V}, V = e_i \cap e_j,\ i,j = 1,\ldots,n_E\}.$$

The solution space is defined to contain the conditions of inextensibility and unshearability as follows:

$$V_S = \{(\mathbf{d},\mathbf{w}) \in H^1(\mathcal{N};\mathbb{R}^6) : \partial_s \mathbf{d}_i + \mathbf{t}_i \times \mathbf{w}_i = 0, i = 1,\ldots,n_E\}. \tag{8}$$

For a function $(\mathbf{d},\mathbf{w}) \in V_S$, we consider the following norms on $H^1(\mathcal{N};\mathbb{R}^3)$:

$$\|\mathbf{d}\|^2_{H^1(\mathcal{N};\mathbb{R}^3)} := \sum_{i=1}^{n_E} \|\mathbf{d}_i\|^2_{H^1(0,l_i;\mathbb{R}^3)}, \quad \|\mathbf{w}\|^2_{H^1(\mathcal{N};\mathbb{R}^3)} := \sum_{i=1}^{n_E} \|\mathbf{w}_i\|^2_{H^1(0,l_i;\mathbb{R}^3)},$$

and the following norms on $L^2(\mathcal{N};\mathbb{R}^3)$:

$$\|\mathbf{d}\|^2_{L^2(\mathcal{N};\mathbb{R}^3)} := \sum_{i=1}^{n_E} \|\mathbf{d}_i\|^2_{L^2(0,l_i;\mathbb{R}^3)}, \quad \|\mathbf{w}\|^2_{L^2(\mathcal{N};\mathbb{R}^3)} := \sum_{i=1}^{n_E} \|\mathbf{w}_i\|^2_{L^2(0,l_i;\mathbb{R}^3)}.$$

The weak formulation for a single curved rod is obtained by first multiplying the first equation in (7) by a test function $\boldsymbol{\xi}$, the second equation in (7) by a test function $\boldsymbol{\zeta}$, and integrating over $[0,l]$ (we are dropping the sub-script i in this calculation). The two equations added together give:

$$\rho_S A \int_0^l \partial_t^2 \mathbf{d}\cdot\boldsymbol{\xi} + \rho_S \int_0^l M\partial_t^2\mathbf{w}\cdot\boldsymbol{\zeta} - \int_0^l \partial_s\mathbf{p}\cdot\boldsymbol{\xi} - \int_0^l \mathbf{f}\cdot\boldsymbol{\xi} \\ - \int_0^l \partial_s\mathbf{q}\cdot\boldsymbol{\zeta} + \int_0^l \mathbf{p}\cdot(\mathbf{t}\times\boldsymbol{\zeta}) = 0.$$

The terms that involve the partial derivative with respect to s can be rewritten by using integration by parts:

$$\rho_S A \int_0^l \partial_t^2 \mathbf{d}\cdot\boldsymbol{\xi} + \rho_S \int_0^l M\partial_t^2\mathbf{w}\cdot\boldsymbol{\zeta} + \int_0^l \mathbf{p}\cdot\partial_s\boldsymbol{\xi} - \mathbf{p}(l)\cdot\boldsymbol{\xi}(l) + \mathbf{p}(0)\cdot\boldsymbol{\xi}(0) \\ - \int_0^l \mathbf{f}\cdot\boldsymbol{\xi} + \int_0^l \mathbf{q}\cdot\partial_s\boldsymbol{\zeta} - \mathbf{q}(l)\cdot\boldsymbol{\zeta}(l) + \mathbf{q}(0)\cdot\boldsymbol{\zeta}(0) + \int_0^l \mathbf{p}\cdot(\mathbf{t}\times\boldsymbol{\zeta}) = 0.$$

Finally, by using the constitutive relation and the condition of inextensibility and unshearability, we obtain the weak formulation for a single rod problem: find $(\mathbf{d}, \mathbf{w})$ such that

$$\begin{aligned} &\rho_S A \int_0^l \partial_t^2 \mathbf{d} \cdot \boldsymbol{\xi} + \rho_S \int_0^l M \partial_t^2 \mathbf{w} \cdot \boldsymbol{\zeta} + \int_0^l Q H Q^T \partial_s \mathbf{w} \cdot \partial_s \boldsymbol{\zeta} \\ &= \int_0^l \mathbf{f} \cdot \boldsymbol{\xi} + \mathbf{p}(l) \cdot \boldsymbol{\xi}(l) - \mathbf{p}(0) \cdot \boldsymbol{\xi}(0) + \mathbf{q}(l) \cdot \boldsymbol{\zeta}(l) - \mathbf{q}(0) \cdot \boldsymbol{\zeta}(0), \end{aligned} \tag{9}$$

for all $(\boldsymbol{\xi}, \boldsymbol{\zeta}) \in H^1(0,l) \times H^1(0,l)$ that satisfy the condition of inextensibility and unshearability.

To get a weak formulation for the mesh net problem, we sum up the weak formulations for each local mesh component (i.e., curved rod, or strut). At each vertex, the boundary terms from (9) involving $\mathbf{p}$ and $\mathbf{q}$ will add up to zero due to the dynamic coupling conditions. The weak formulation for the mesh net problem then reads: find $(\mathbf{d}, \mathbf{w}) \in V_S$ such that

$$\begin{aligned} &\rho_S \sum_{i=1}^{n_E} A_i \int_0^{l_i} \partial_t^2 \mathbf{d}_i \cdot \boldsymbol{\xi}_i + \rho_S \sum_{i=1}^{n_E} \int_0^{l_i} M_i \partial_t^2 \mathbf{w}_i \cdot \boldsymbol{\zeta}_i \\ &+ \sum_{i=1}^{n_E} \int_0^{l_i} Q_i H_i Q_i^T \partial_s \mathbf{w}_i \cdot \partial_s \boldsymbol{\zeta}_i = \sum_{i=1}^{n_E} \int_0^{l_i} \mathbf{f}_i \cdot \boldsymbol{\xi}_i, \end{aligned} \tag{10}$$

for all test functions $(\boldsymbol{\xi}, \boldsymbol{\zeta}) = ((\boldsymbol{\xi}_1, \boldsymbol{\zeta}_1), \ldots, (\boldsymbol{\xi}_{n_E}, \boldsymbol{\zeta}_{n_E})) \in V_S$.

2.4. Koiter shell and 1D mesh problem coupling

We will be assuming that the elastic mesh is always confined to the shell surface so that the following holds:

$$\bigcup_{i=1}^{n_E} \mathbf{P}_i([0, l_i]) \subset \Gamma = \boldsymbol{\varphi}(\overline{\omega}).$$

Since $\boldsymbol{\varphi}$ is injective on ω, functions $\boldsymbol{\pi}_i$, denoting the reparameterizations of the stent struts:

$$\boldsymbol{\pi}_i = \boldsymbol{\varphi}^{-1} \circ \mathbf{P}_i : [0, l_i] \to \overline{\omega}, \quad i = 1, \ldots, n_E,$$

are well defined. The reference configuration of the mesh defined on ω will be denoted by $\omega_S = \bigcup_{i=1}^{n_E} \boldsymbol{\pi}_i([0, l_i])$, and of the mesh defined on Γ will be denoted by $\Gamma_S = \bigcup_{i=1}^{n_E} \mathbf{P}_i([0, l_i])$. See Fig. 1.

The elastic mesh and the shell are coupled through the kinematic and dynamic coupling conditions. The kinematic coupling condition states that the displacement of the shell at the point $(R\cos\theta, R\sin\theta, z) \in \Gamma$, which is associated with the point $(z, \theta) \in \omega_S$ via the mapping $\boldsymbol{\varphi}$, is equal to the displacement of the stent at the point $s_i = \boldsymbol{\pi}_i^{-1}(z, \theta)$, that is associated with the same point $(z, \theta) \in \omega_S$ via the mapping $\boldsymbol{\pi}_i$. For a point $s_i \in [0, l_i]$ such that $\boldsymbol{\pi}_i(s_i) = (z, \theta) \in \omega_S$, the kinematic coupling condition reads:

$$\boldsymbol{\eta}(t, \boldsymbol{\pi}_i(s_i)) = \mathbf{d}_i(t, s_i). \tag{11}$$

The dynamic coupling condition describes the balance of forces. The force exerted by the Koiter shell onto the mesh is balanced by the force exerted by the mesh onto the Koiter shell. More precisely, let $J_i = \boldsymbol{\pi}_i([0, l_i])$, and

$$\langle \delta_{J_i}, f \rangle = \int_{J_i} f \, d\gamma_i, \quad i = 1, \ldots, n_E,$$

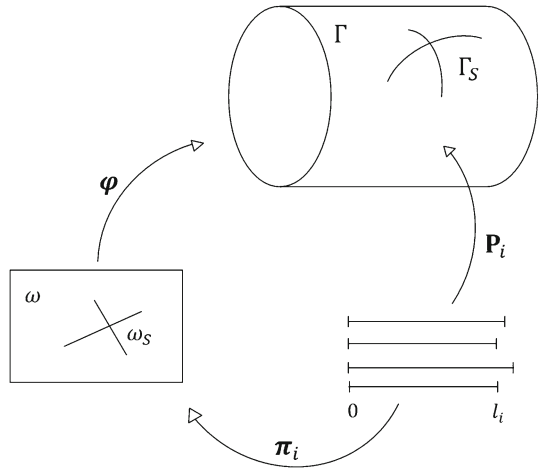

FIG. 1. Parameterization of the mesh struts

where $d\gamma_i$ is the curve element associated with the parameterization $\boldsymbol{\pi}_i$. The weak formulation of the shell (5) can then be written as:

$$\begin{aligned}\rho_K h \int_\omega \partial_t^2 \boldsymbol{\eta}\cdot\boldsymbol{\psi} R + \langle \mathcal{L}\boldsymbol{\eta}, \boldsymbol{\psi}\rangle &= \sum_{i=1}^{n_E} \langle \delta_{J_i}, \mathbf{f}\cdot\boldsymbol{\psi} R\rangle \\ &= \sum_{i=1}^{n_E} \int_{J_i} \mathbf{f}(z,\theta)\cdot\boldsymbol{\psi}(z,\theta) R d\gamma_i \\ &= \sum_{i=1}^{n_E} \int_0^{l_i} \mathbf{f}(\boldsymbol{\pi}_i(s))\cdot\boldsymbol{\psi}(\boldsymbol{\pi}_i(s))\|\boldsymbol{\pi}_i'(s)\| R \mathrm{d}s.\end{aligned}$$

If we denote by $\mathbf{f}_i$ the force exerted by the i-th mesh strut onto the shell, by force balance, the right-hand side has to be equal to $-\sum_{i=1}^{n_E}\int_0^{l_i}\mathbf{f}_i(s)\cdot\boldsymbol{\xi}_i(s)ds$. Thus, $\mathbf{f}(\boldsymbol{\pi}_i(s_i))\|\boldsymbol{\pi}_i'(s_i)\|R = -\mathbf{f}_i(s_i)$, i.e., $\mathbf{f}(\boldsymbol{\pi}_i(s_i))R = -\dfrac{\mathbf{f}_i(s_i)}{\|\boldsymbol{\pi}_i'(s_i)\|}$, $s_i \in (0, l_i)$. For a point $(z,\theta) = \boldsymbol{\pi}_i(s_i) \in \omega_S$, which came from an $s_i \in (0,l_i)$, the dynamic coupling condition reads: $\mathbf{f}R = -\dfrac{\mathbf{f}_i\circ\boldsymbol{\pi}_i^{-1}}{\|\boldsymbol{\pi}_i'\circ\boldsymbol{\pi}_i^{-1}\|}$. For an arbitrary point $(z,\theta)\in\omega$, the dynamic coupling condition reads:

$$\mathbf{f}R = -\sum_{i=1}^{n_E} \frac{\mathbf{f}_i\circ\boldsymbol{\pi}_i^{-1}}{\|\boldsymbol{\pi}_i'\circ\boldsymbol{\pi}_i^{-1}\|}\delta_{J_i}. \tag{12}$$

Now, the weak formulation for the coupled mesh–shell problem reads:

$$\rho_K h \int_\omega \partial_t^2\boldsymbol{\eta}\cdot\boldsymbol{\psi} R + \langle \mathcal{L}\boldsymbol{\eta},\boldsymbol{\psi}\rangle = -\sum_{i=1}^{n_E}\langle \delta_{J_i}, \frac{\mathbf{f}_i\circ\boldsymbol{\pi}_i^{-1}}{\|\boldsymbol{\pi}_i'\circ\boldsymbol{\pi}_i^{-1}\|}\boldsymbol{\psi}\rangle, \tag{13}$$

for all test functions $\boldsymbol{\psi}\in V_K$. Here, $\mathbf{f}_i$'s are defined in (10), where the test functions $\boldsymbol{\xi}_i$ are such that $\boldsymbol{\psi}\circ\boldsymbol{\pi}_i = \boldsymbol{\xi}_i$. The coupled mesh–shell weak solution space is given by:

$$V_{KS} = \{(\boldsymbol{\eta},\mathbf{d},\mathbf{w})\in V_K\times V_S : \boldsymbol{\eta}\circ\boldsymbol{\pi} = \mathbf{d} \text{ on } \prod_{i=1}^{n_E}(0,l_i)\},$$

where we denoted $\boldsymbol{\eta} \circ \boldsymbol{\pi} = (\boldsymbol{\eta} \circ \boldsymbol{\pi}_1, \ldots, \boldsymbol{\eta} \circ \boldsymbol{\pi}_{n_E})$.

The *dynamic* coupled mesh–shell problem presented here is an extension of the coupled mesh–shell problem first studied in [12] for the static case.

2.5. The fluid–composite structure coupling

From now on, by 'structure' we will refer to the Koiter shell coupled with the 1D elastic mesh described above. The coupling between the fluid and the structure is defined by two sets of coupling conditions: the kinematic and dynamic coupling conditions, satisfied at the fixed, lateral boundary Γ, giving rise to a linear fluid–structure coupling. The coupling conditions impose continuity of velocity and balance of contact forces. Let us emphasize that in our work, the dynamic coupling condition also reflects the presence of a 1D elastic mesh at the fluid–structure interface. The coupling conditions read:

- The kinematic condition: $\partial_t \boldsymbol{\eta} = \mathbf{u}|_\Gamma \circ \boldsymbol{\varphi}$ on $(0,T) \times \omega$,
- The dynamic condition:

$$\rho_K h \partial_t^2 \boldsymbol{\eta} R + \mathcal{L}\boldsymbol{\eta} + \sum_{i=1}^{n_E} \frac{\mathbf{f}_i \circ \boldsymbol{\pi}_i^{-1}}{\|\boldsymbol{\pi}_i' \circ \boldsymbol{\pi}_i^{-1}\|} \delta_{J_i} = -J(\boldsymbol{\sigma} \circ \boldsymbol{\varphi})(\mathbf{n} \circ \boldsymbol{\varphi}), \text{ on } (0,T) \times \omega,$$

where J denotes the Jacobian of the transformation from cylindrical to Cartesian coordinates, and $\mathbf{n}$ denotes the outer unit normal on Γ. For the linear fluid–structure interaction problem considered here, the Jacobian J is equal to R.

In summary, we study the following fluid–structure interaction problem:

Problem 1. Find $(\mathbf{u}, p, \boldsymbol{\eta}, \mathbf{d}, \mathbf{w})$ such that

$$\left.\begin{aligned} \rho_F \partial_t \mathbf{u} &= \nabla \cdot \boldsymbol{\sigma} \\ \nabla \cdot \mathbf{u} &= 0 \end{aligned}\right\} \text{ in } (0,T) \times \Omega, \tag{14}$$

$$\left.\begin{aligned} \partial_t \boldsymbol{\eta} &= \mathbf{u} \circ \boldsymbol{\varphi} \\ \rho_K h \partial_t^2 \boldsymbol{\eta} R + \mathcal{L}\boldsymbol{\eta} + \sum_{i=1}^{n_E} \frac{\mathbf{f}_i \circ \boldsymbol{\pi}_i^{-1}}{\|\boldsymbol{\pi}_i' \circ \boldsymbol{\pi}_i^{-1}\|} \delta_{J_i} &= -J(\boldsymbol{\sigma} \circ \boldsymbol{\varphi})(\mathbf{n} \circ \boldsymbol{\varphi}) \end{aligned}\right\} \text{ on } (0,T) \times \omega, \tag{15}$$

$$\left.\begin{aligned} \rho_S A_i \partial_t^2 \mathbf{d}_i &= \partial_s \mathbf{p}_i + \mathbf{f}_i \\ \rho_S M_i \partial_t^2 \mathbf{w}_i &= \partial_s \mathbf{q}_i + \mathbf{t}_i \times \mathbf{p}_i \\ 0 &= \partial_s \mathbf{w}_i - Q_i H_i^{-1} Q_i^T \mathbf{q}_i \\ 0 &= \partial_s \mathbf{d}_i + \mathbf{t}_i \times \mathbf{w}_i \end{aligned}\right\} \text{ on } (0,T) \times (0,l_i). \tag{16}$$

Problem (14)–(16) is supplemented with the following set of boundary and the initial conditions:

$$\begin{cases} p = P_{\text{in/out}}(t), & \text{on } (0,T) \times \Gamma_{\text{in/out}}, \\ \mathbf{u} \times \mathbf{e}_z = 0, & \text{on } (0,T) \times \Gamma_{\text{in/out}}, \\ \boldsymbol{\eta}(t,0,\theta) = \boldsymbol{\eta}(t,L,\theta) = 0, & \text{on } (0,T) \times (0,2\pi), \\ \partial_z \eta_r(t,0,\theta) = \partial_z \eta_r(t,L,\theta) = 0, & \text{on } (0,T) \times (0,2\pi), \\ \boldsymbol{\eta}(t,z,0) = \boldsymbol{\eta}(t,z,2\pi), & \text{on } (0,T) \times (0,L), \\ \partial_\theta \eta_r(t,z,0) = \partial_\theta \eta_r(t,z,2\pi), & \text{on } (0,T) \times (0,L), \end{cases} \tag{17}$$

$$\mathbf{u}(0) = \mathbf{u}_0,\ \boldsymbol{\eta}(0) = \boldsymbol{\eta}_0,\ \partial_t \boldsymbol{\eta}(0) = \boldsymbol{v}_0, \mathbf{d}_i(0) = \mathbf{d}_{0i},\ \partial_t \mathbf{d}_i(0) = \mathbf{k}_{0i},\ \mathbf{w}_i(0) = \mathbf{w}_{0i},\ \partial_t \mathbf{w}_i(0) = \mathbf{z}_{0i}. \tag{18}$$

3. The energy of the coupled fluid–mesh–shell problem

We formally prove that problem (14)–(16) satisfies the following energy inequality:

$$\frac{\mathrm{d}}{\mathrm{d}t}E(t) + D(t) \leq C(P_{\mathrm{in}}(t), P_{\mathrm{out}}(t)), \tag{19}$$

where $E(t)$ denotes the total energy of the coupled problem (the sum of the kinetic and elastic energy), $D(t)$ denotes dissipation due to fluid viscosity, and $C(P_{\mathrm{in}}(t), P_{\mathrm{out}}(t))$ is a constant which depends only on the L^2-norms of the inlet and outlet pressure data. More precisely, if we denote by $\|\mathbf{w}\|_m$ and $\|\mathbf{w}\|_r$ the following norms associated with the elastic energy of the elastic mesh:

$$\|\mathbf{w}\|_m^2 := \sum_{i=1}^{n_E} \|\mathbf{w}_i\|_m^2 = \sum_{i=1}^{n_E} \int_0^{l_i} M_i \mathbf{w}_i \cdot \mathbf{w}_i,$$

$$\|\mathbf{w}\|_r^2 := \sum_{i=1}^{n_E} \|\mathbf{w}_i\|_r^2 = \sum_{i=1}^{n_E} \int_0^{l_i} Q_i H_i Q_i^T \partial_s \mathbf{w}_i \cdot \partial_s \mathbf{w}_i,$$

and by $\|\boldsymbol{\eta}\|_{L^2(R;\omega)}$ the weighted L^2 norm on ω, with the weight R associated with the geometry of the Koiter shell (Jacobian):

$$\|\boldsymbol{\eta}\|_{L^2(R;\omega)}^2 := \int_\omega |\boldsymbol{\eta}|^2 R \, \mathrm{d}\omega,$$

then the total energy of the coupled FSI problem is defined by

$$E(t) = \frac{\rho_F}{2}\|\mathbf{u}\|_{L^2(\Omega)}^2 + \frac{\rho_K h}{2}\|\partial_t \boldsymbol{\eta}\|_{L^2(R;\omega)}^2 + \frac{\rho_S}{2}\sum_{i=1}^{n_E} A_i \|\partial_t \mathbf{d}_i\|_{L^2(0,l_i)}^2$$
$$+ \frac{\rho_S}{2}\|\partial_t \mathbf{w}\|_m^2 + \frac{1}{2}\langle \mathcal{L}\boldsymbol{\eta}, \boldsymbol{\eta}\rangle + \|\mathbf{w}\|_r^2,$$

while $D(t)$ is given by

$$D(t) = 2\mu_F \|\mathbf{D}(\mathbf{u})\|_{L^2(\Omega)}^2.$$

Notice that the norm $\|\cdot\|_m$ is equivalent to the standard $L^2(\mathcal{N})$ norm.

Proposition 3.1. *There exists a constant $C > 0$ such that*

$$\|\mathbf{w}\|_r^2 \leq C\|\mathbf{w}\|_{H^1(\mathcal{N})}^2.$$

Proof. Since Q_i is orthogonal and H_i positive definite, for each $i = 1, \ldots, n_E$, the following inequality holds:

$$\|\mathbf{w}_i\|_r^2 = \int_0^{l_i} Q_i H_i Q_i^T \partial_s \mathbf{w}_i \cdot \partial_s \mathbf{w}_i = \int_0^{l_i} H_i Q_i^T \partial_s \mathbf{w}_i \cdot Q_i^T \partial_s \mathbf{w}_i$$
$$\leq \int_0^{l_i} \lambda_{\max}(H_i) Q_i^T \partial_s \mathbf{w}_i \cdot Q_i^T \partial_s \mathbf{w}_i = \lambda_{\max}(H_i)\|Q_i^T \partial_s \mathbf{w}_i\|_{L^2(0,l_i)}^2$$
$$= \lambda_{\max}(H_i)\|\partial_s \mathbf{w}_i\|_{L^2(0,l_i)}^2 \leq \lambda_{\max}(H_i)\left(\|\partial_s \mathbf{w}_i\|_{L^2(0,l_i)}^2 + \|\mathbf{w}_i\|_{L^2(0,l_i)}^2\right)$$
$$\leq \lambda_{\max}(H_i)\|\mathbf{w}_i\|_{H^1(0,l_i)}^2,$$

where $\lambda_{\max}(H_i)$ is the maximum eigenvalue of matrix H_i. □

To derive the energy inequality (19), we first multiply the first equation in (1) by $\mathbf{u}$ and integrate by parts over Ω to obtain:

$$\begin{aligned}
&\int_\Omega \rho_F \partial_t \mathbf{u}\cdot\mathbf{u} - \int_\Omega \nabla\cdot(-pI+2\mu_F\mathbf{D}(\mathbf{u}))\cdot\mathbf{u}\\
&= \frac{\rho_F}{2}\frac{\mathrm{d}}{\mathrm{d}t}\int_\Omega |\mathbf{u}|^2 - \int_\Omega \nabla\cdot((-pI+2\mu_F\mathbf{D}(\mathbf{u}))\mathbf{u}) + \int_\Omega (-pI+2\mu_F\mathbf{D}(\mathbf{u})):\nabla\mathbf{u}\\
&= \frac{\rho_F}{2}\frac{\mathrm{d}}{\mathrm{d}t}\int_\Omega |\mathbf{u}|^2 - \int_{\partial\Omega}(-pI+2\mu_F\mathbf{D}(\mathbf{u}))\mathbf{n}\cdot\mathbf{u} - \int_\Omega pI:\nabla\mathbf{u} + 2\mu_F\int_\Omega \mathbf{D}(\mathbf{u}):\nabla\mathbf{u}\\
&= \frac{\rho_F}{2}\frac{\mathrm{d}}{\mathrm{d}t}\int_\Omega |\mathbf{u}|^2 - \int_{\partial\Omega}(-pI+2\mu_F\mathbf{D}(\mathbf{u}))\mathbf{n}\cdot\mathbf{u} - \int_\Omega p\nabla\cdot\mathbf{u} + 2\mu_F\int_\Omega \mathbf{D}(\mathbf{u}):\mathbf{D}(\mathbf{u})\\
&= \frac{\rho_F}{2}\frac{\mathrm{d}}{\mathrm{d}t}\int_\Omega |\mathbf{u}|^2 - \int_{\partial\Omega}(-pI+2\mu_F\mathbf{D}(\mathbf{u}))\mathbf{n}\cdot\mathbf{u} + 2\mu_F\int_\Omega |\mathbf{D}(\mathbf{u})|^2,
\end{aligned}$$

where we have used $\nabla\mathbf{u}:\nabla\mathbf{u} = \mathrm{tr}(\nabla\mathbf{u}\nabla^T\mathbf{u}) = \mathrm{tr}(\nabla^T\mathbf{u}\nabla\mathbf{u}) = \nabla^T\mathbf{u}:\nabla^T\mathbf{u}$.
To calculate the boundary integral over $\partial\Omega$, we first notice that on $\Gamma_{\mathrm{in/out}}$ the boundary condition $\mathbf{u}\times\mathbf{e}_z = 0$ gives $u_x = u_y = 0$. Using divergence-free condition, we also obtain $\partial_z u_z = 0$. Now, since the normal to $\Gamma_{\mathrm{in/out}}$ is equal to $\mathbf{n} = (\mp 1, 0, 0)$, we get:

$$\begin{aligned}
&-\int_{\partial\Omega}(-pI+2\mu_F\mathbf{D}(\mathbf{u}))\mathbf{n}\cdot\mathbf{u}\\
&= -\int_\Gamma \boldsymbol{\sigma}\mathbf{n}\cdot\mathbf{u} - \int_{\Gamma_{\mathrm{in}}\cup\Gamma_{\mathrm{out}}}(-pI+2\mu_F\mathbf{D}(\mathbf{u}))\mathbf{n}\cdot\mathbf{u}\\
&= -\int_\Gamma \boldsymbol{\sigma}\mathbf{n}\cdot\mathbf{u} - \int_{\Gamma_{\mathrm{in}}} pu_z + \int_{\Gamma_{\mathrm{out}}} pu_z.
\end{aligned} \tag{20}$$

To calculate the boundary integral over Γ we first multiply the Koiter shell equation (6) by $\partial_t\boldsymbol{\eta}$ and integrate over ω:

$$\begin{aligned}
\int_\omega \mathbf{f}\cdot\partial_t\boldsymbol{\eta}R &= \rho_K h\int_\omega \partial_t^2\boldsymbol{\eta}\cdot\partial_t\boldsymbol{\eta}R + \langle\mathcal{L}\boldsymbol{\eta},\partial_t\boldsymbol{\eta}\rangle\\
&= \frac{\rho_K h}{2}\frac{\mathrm{d}}{\mathrm{d}t}\int_\omega \partial_t\boldsymbol{\eta}\cdot\partial_t\boldsymbol{\eta}R + \frac{1}{2}\frac{\mathrm{d}}{\mathrm{d}t}\langle\mathcal{L}\boldsymbol{\eta},\boldsymbol{\eta}\rangle\\
&= \frac{\rho_K h}{2}\frac{\mathrm{d}}{\mathrm{d}t}\|\partial_t\boldsymbol{\eta}\|^2_{L^2(R;\omega)} + \frac{1}{2}\frac{\mathrm{d}}{\mathrm{d}t}\langle\mathcal{L}\boldsymbol{\eta},\boldsymbol{\eta}\rangle.
\end{aligned}$$

Next, we want to use $(\partial_t\mathbf{d}_i, \partial_t\mathbf{w}_i), i = 1,\dots,n_E$, as test functions in the weak formulation for the mesh problem (10). Before doing so, we need to check if these test functions are *admissible*, i.e., if they satisfy the condition of inextensibility and unshearability $\partial_s\mathbf{d}_i + \mathbf{t}_i\times\mathbf{w}_i = 0, i = 1,\dots,n_E$. We differentiate this condition with respect to t and use the fact that $\mathbf{t}_i$ do not depend on t, to obtain

$$\partial_s(\partial_t\mathbf{d}_i) + \mathbf{t}_i\times(\partial_t\mathbf{w}_i) = 0, \quad i = 1,\dots,n_E,$$

which implies that, indeed, $(\partial_t\mathbf{d}_i, \partial_t\mathbf{w}_i)\in V_S,\ i = 1,\dots,n_E$.

By using $(\partial_t \mathbf{d}, \partial_t \mathbf{w}) = ((\partial_t \mathbf{d}_1, \partial_t \mathbf{w}_1), \ldots, (\partial_t \mathbf{d}_{n_E}, \partial_t \mathbf{w}_{n_E}))$ as a test function in the weak formulation for the mesh problem, we obtain:

$$\begin{aligned}\sum_{i=1}^{n_E} \int_0^{l_i} \mathbf{f}_i \cdot \partial_t \mathbf{d}_i &= \rho_S \sum_{i=1}^{n_E} A_i \int_0^{l_i} \partial_t^2 \mathbf{d}_i \cdot \partial_t \mathbf{d}_i + \rho_S \sum_{i=1}^{n_E} \int_0^{l_i} M_i \partial_t^2 \mathbf{w}_i \cdot \partial_t \mathbf{w}_i \\ &\quad + \sum_{i=1}^{n_E} \int_0^{l_i} Q_i H_i Q_i^T \partial_s \mathbf{w}_i \cdot \partial_s \partial_t \mathbf{w}_i \\ &= \frac{\rho_S}{2} \frac{\mathrm{d}}{\mathrm{d}t} \sum_{i=1}^{n_E} A_i \|\partial_t \mathbf{d}_i\|^2_{L^2(0,l_i)} + \frac{\rho_S}{2} \frac{\mathrm{d}}{\mathrm{d}t} \sum_{i=1}^{n_E} \|\partial_t \mathbf{w}_i\|^2_m \\ &\quad + \frac{\mathrm{d}}{\mathrm{d}t} \sum_{i=1}^{n_E} \|\mathbf{w}_i\|^2_r.\end{aligned}$$

By enforcing the kinematic and dynamic boundary conditions on Γ, and recalling that the Jacobian of the transformation between Γ and ω is $J = R$, we obtain:

$$\begin{aligned}-\int_\Gamma \boldsymbol{\sigma}\mathbf{n} \cdot \mathbf{u} &= -\int_\omega J(\boldsymbol{\sigma} \circ \boldsymbol{\varphi})(\mathbf{n} \circ \boldsymbol{\varphi}) \cdot \partial_t \boldsymbol{\eta} = \int_\omega \mathbf{f} \cdot \partial_t \boldsymbol{\eta} R + \sum_{i=1}^{n_E} \int_{J_i} \frac{\mathbf{f}_i \circ \boldsymbol{\pi}_i^{-1}}{\|\boldsymbol{\pi}_i' \circ \boldsymbol{\pi}_i^{-1}\|} \delta_{J_i} \cdot \partial_t \boldsymbol{\eta} \\ &= \int_\omega \mathbf{f} \cdot \partial_t \boldsymbol{\eta} R + \sum_{i=1}^{n_E} \int_0^{l_i} \mathbf{f}_i \cdot \partial_t \boldsymbol{\eta} \circ \boldsymbol{\pi}_i = \int_\omega \mathbf{f} \cdot \partial_t \boldsymbol{\eta} R + \sum_{i=1}^{n_E} \int_0^{l_i} \mathbf{f}_i \cdot \partial_t \mathbf{d}_i.\end{aligned} \tag{21}$$

By inserting the expressions for $\mathbf{f}$ and $\mathbf{f}_i$ from the shell and mesh problems into (21), we get:

$$\begin{aligned}-\int_\Gamma \boldsymbol{\sigma}\mathbf{n} \cdot \mathbf{u} f &= \frac{\rho_K h}{2} \frac{\mathrm{d}}{\mathrm{d}t} \|\partial_t \boldsymbol{\eta}\|^2_{L^2(R;\omega)} + \frac{1}{2} \frac{\mathrm{d}}{\mathrm{d}t} \langle \mathcal{L}\boldsymbol{\eta}, \boldsymbol{\eta} \rangle \\ &\quad + \frac{\rho_S}{2} \frac{\mathrm{d}}{\mathrm{d}t} \sum_{i=1}^{n_E} A_i \|\partial_t \mathbf{d}_i\|^2_{L^2(0,l_i)} + \frac{\rho_S}{2} \frac{\mathrm{d}}{\mathrm{d}t} \sum_{i=1}^{n_E} \|\partial_t \mathbf{w}_i\|^2_m + \frac{\mathrm{d}}{\mathrm{d}t} \sum_{i=1}^{n_E} \|\mathbf{w}_i\|^2_r.\end{aligned} \tag{22}$$

Finally, by replacing the trace of the normal stress on Γ in (20) by (22), one obtains the following energy equality:

$$\begin{aligned}&\frac{\rho_F}{2} \frac{\mathrm{d}}{\mathrm{d}t} \|\mathbf{u}\|^2_{L^2(\Omega)} + 2\mu_F \|\mathbf{D}(\mathbf{u})\|^2_{L^2(\Omega)} + \frac{\rho_K h}{2} \frac{\mathrm{d}}{\mathrm{d}t} \|\partial_t \boldsymbol{\eta}\|^2_{L^2(R;\omega)} \\ &\quad + \frac{1}{2} \frac{\mathrm{d}}{\mathrm{d}t} \langle \mathcal{L}\boldsymbol{\eta}, \boldsymbol{\eta} \rangle + \frac{\rho_S}{2} \frac{\mathrm{d}}{\mathrm{d}t} \sum_{i=1}^{n_E} A_i \|\partial_t \mathbf{d}_i\|^2_{L^2(0,l_i)} + \frac{\rho_S}{2} \frac{\mathrm{d}}{\mathrm{d}t} \sum_{i=1}^{n_E} \|\partial_t \mathbf{w}_i\|^2_m \\ &\quad + \frac{\mathrm{d}}{\mathrm{d}t} \sum_{i=1}^{n_E} \|\mathbf{w}_i\|^2_r = \int_{\Gamma_{\text{in}}} p u_z - \int_{\Gamma_{\text{out}}} p u_z.\end{aligned} \tag{23}$$

The right-hand side is equal to

$$\int_{\Gamma_{\text{in}}} P_{\text{in}}(t) u_z - \int_{\Gamma_{\text{out}}} P_{\text{out}}(t) u_z.$$

Using the trace theorem, Korn inequality and Cauchy inequality (with ε), one can estimate:

$$\left| \int\limits_{\Gamma_{\text{in/out}}} P_{\text{in/out}}(t) u_z \right| \leq C|P_{\text{in/out}}| \|\mathbf{u}\|_{H^1(\Omega)} \leq C|P_{\text{in/out}}| \|\mathbf{D}(\mathbf{u})\|_{L^2(\Omega)}$$
$$\leq \frac{C}{2\varepsilon}|P_{\text{in/out}}|^2 + \frac{C\varepsilon}{2}\|\mathbf{D}(\mathbf{u})\|^2_{L^2(\Omega)}.$$

We note that, indeed, the fluid velocity $\mathbf{u}$ satisfies the conditions for Korn inequality (Theorem 6.3–4 in [20]). Namely, the boundary condition $\mathbf{u} \times \mathbf{e}_z = 0$ on $\Gamma_{\text{in/out}}$ gives us $u_x = u_y = 0$ and $\partial_z u_z = 0$. Using the kinematic coupling condition $u_z = \partial_t \eta_z$ (on ω), we obtain that $u_z = 0$, so $\mathbf{u} = 0$ on $\Gamma_{\text{in/out}}$. Finally, by choosing ε such that $\frac{C\varepsilon}{2} \leq \mu_F$, we get the energy inequality (19).

4. The operator splitting scheme

Our goal is to approximate the coupled FSI problem using time-discretization via operator splitting, and then prove that solutions to the approximate problems converge to a weak solution of the continuous problem, as the time-discretization step tends to zero.

We use the Lie splitting scheme which can be summarized as follows. Let $N \in \mathbb{N}, \Delta t = T/N$ and $t_n = n\Delta t$. Consider the following initial-value problem

$$\frac{\mathrm{d}\phi}{\mathrm{d}t} + A\phi = 0 \quad \text{in} \quad (0, T),$$
$$\phi(0) = \phi_0,$$

where A is an operator defined on a Hilbert space, and A can be written as $A = A_1 + A_2$. Set $\phi^0 = \phi_0$ and for $n = 0, \ldots, N-1, i = 1, 2$, compute $\phi^{n+\frac{i}{2}}$ by solving

$$\frac{\mathrm{d}\phi_i}{\mathrm{d}t} + A_i\phi_i = 0 \quad \text{in} \quad (t_n, t_{n+1}),$$
$$\phi_i(t_n) = \phi^{n+\frac{i-1}{2}},$$

and then set $\phi^{n+\frac{i}{2}} = \phi_i(t_{n+1})$.

To perform the time-discretization via operator splitting, we need to rewrite our FSI problem as a first-order system in time. This will be done by replacing the second-order time derivative of $\boldsymbol{\eta}$, with the first-order time derivative of the Koiter shell velocity $\boldsymbol{v} = \partial_t \boldsymbol{\eta}$, by replacing the second-order time derivative of $\mathbf{d}$ by the first-order time derivative of the mesh velocity $\mathbf{k} = \partial_t \mathbf{d}$, and by replacing the second-order time derivative of $\mathbf{w}$ by the first-order time derivative of the rotation velocity $\mathbf{z} = \partial_t \mathbf{w}$.

We apply this approach to split Problem 1 into a fluid and a structure subproblem, and then

1. Solve the structure subproblem on (t_n, t_{n+1}) using for the initial data the solution of the fluid subproblem from the previous time step, and then
2. Solve the fluid subproblem on (t_n, t_{n+1}) using for the initial data the solution of the just calculated structure subproblem.

There are many different ways to split the coupled problem into a fluid and a structure subproblem. Only certain splitting strategies would lead to a stable and convergent scheme. Here, we define a structure and a fluid subproblem for the Lie splitting scheme that will, indeed, provide a convergent scheme, converging to a weak solution of the coupled, continuous problem.

4.1. The structure subproblem

In this step, we solve an elastodynamics problem for the location of the deformable boundary, which is defined by the dynamic coupling condition involving only the elastic energy of the structure. The motion of the structure is driven by the initial velocity of the structure, obtained, using the kinematic coupling condition, from the trace of the fluid velocity calculated in the previous time step. The fluid velocity $\mathbf{u}$ remains unchanged in this step. The structure subproblem reads: for a given $(\mathbf{u}^n, \boldsymbol{\eta}^n, \boldsymbol{v}^n, \mathbf{d}^n, \mathbf{w}^n, \mathbf{k}^n, \mathbf{z}^n)$, calculated in the previous time step, find $(\mathbf{u}, \boldsymbol{\eta}, \boldsymbol{v}, \mathbf{d}, \mathbf{w}, \mathbf{k}, \mathbf{z})$ such that

$$
\begin{aligned}
&\partial_t \mathbf{u} = 0, \quad \text{in} \quad (t_n, t_{n+1}) \times \Omega,\\
&\begin{cases}
\rho_K h \partial_t \boldsymbol{v} R + \mathcal{L}\boldsymbol{\eta} + \rho_S \displaystyle\sum_{i=1}^{n_E} A_i \frac{\partial_t \mathbf{k}_i \circ \boldsymbol{\pi}_i^{-1}}{\|\boldsymbol{\pi}_i \circ \boldsymbol{\pi}_i^{-1}\|} \delta_{J_i} + \rho_S \displaystyle\sum_{i=1}^{n_E} M_i \frac{\partial_t \mathbf{z}_i \circ \boldsymbol{\pi}_i^{-1}}{\|\boldsymbol{\pi}_i \circ \boldsymbol{\pi}_i^{-1}\|} \delta_{J_i}\\
\quad + \displaystyle\sum_{i=1}^{n_E} Q_i H_i Q_i^T \frac{\partial_s \mathbf{w}_i \circ \boldsymbol{\pi}_i^{-1}}{\|\boldsymbol{\pi}_i \circ \boldsymbol{\pi}_i^{-1}\|} \delta_{J_i} = 0, \quad \text{in} \quad (t_n, t_{n+1}) \times \omega,\\
\boldsymbol{\eta} \circ \boldsymbol{\pi}_i = \mathbf{d}_i, \quad \text{in} \quad (t_n, t_{n+1}) \times (0, l_i), \quad i = 1, \ldots, n_E,
\end{cases}\\
&\begin{cases}
\partial_t \boldsymbol{\eta} = \boldsymbol{v}, \quad \text{in} \quad (t_n, t_{n+1}) \times \omega,\\
\partial_t \mathbf{d}_i = \mathbf{k}_i, \quad \text{in} \quad (t_n, t_{n+1}) \times (0, l_i), \quad i = 1, \ldots n_E,\\
\partial_t \mathbf{w}_i = \mathbf{z}_i, \quad \text{in} \quad (t_n, t_{n+1}) \times (0, l_i), \quad i = 1, \ldots, n_E,\\
\partial_s \mathbf{d}_i + \mathbf{t}_i \times \mathbf{w}_i = 0, \quad \text{in} \quad (t_n, t_{n+1}) \times (0, l_i), \quad i = 1, \ldots, n_E,
\end{cases}
\end{aligned}
$$

with boundary data:

$$
\begin{cases}
\boldsymbol{\eta}(t,0,\theta) = \boldsymbol{\eta}(t,L,\theta) = \partial_z \eta_r(t,0,\theta) = \partial_z \eta_r(t,L,\theta) = 0, \quad \text{on} \quad (t_n, t_{n+1}) \times (0, 2\pi),\\
\boldsymbol{\eta}(t,z,0) = \boldsymbol{\eta}(t,z,2\pi), \;\; \partial_\theta \eta_r(t,z,0) = \partial_\theta \eta_r(t,z,2\pi), \quad \text{on} \quad (t_n, t_{n+1}) \times (0, L),
\end{cases}
$$

and initial data:

$$
\begin{cases}
\mathbf{u}(t_n) = \mathbf{u}^n, \boldsymbol{\eta}(t_n) = \boldsymbol{\eta}^n, \boldsymbol{v}(t_n) = \boldsymbol{v}^n, \mathbf{d}(t_n) = \mathbf{d}^n,\\
\mathbf{w}(t_n) = \mathbf{w}^n, \mathbf{k}(t_n) = \mathbf{k}^n, \mathbf{z}(t_n) = \mathbf{z}^n.
\end{cases}
$$

Then, set $\mathbf{u}^{n+1/2} = \mathbf{u}(t_{n+1}), \boldsymbol{\eta}^{n+1/2} = \boldsymbol{\eta}(t_{n+1}), \boldsymbol{v}^{n+1/2} = \boldsymbol{v}(t_{n+1}), \mathbf{d}^{n+1/2} = \mathbf{d}(t_{n+1}), \mathbf{w}^{n+1/2} = \mathbf{w}(t_{n+1})$, $\mathbf{k}^{n+1/2} = \mathbf{k}(t_{n+1}), \mathbf{z}^{n+1/2} = \mathbf{z}(t_{n+1})$.

4.2. The fluid subproblem

In this step, we solve the Stokes equations for the fluid, with a Robin-type boundary condition on Γ, which is obtained by using the remaining part of the dynamic coupling condition, not used in the structure subproblem. Thus, the boundary condition involves the first-order time derivative term corresponding to the shell inertia, and the trace of the fluid normal stress on Γ. Since the fluid and the elastic mesh "feel" each other only through the motion of the shell, meaning that the fluid motion affects the shell motion, and then the shell motion affects the mesh motion whose elastodynamics is influenced by the presence of the mesh, we *exclude* the mesh from the fluid subproblem. Namely, since we are working with weak solutions of Leray type, the fluid velocity has no trace on the mesh domain since it is a one-dimensional set. Thus, in this step, the structure displacement, the velocity of the mesh displacement,

and the velocity of infinitesimal rotation of cross sections remain unchanged. The fluid subproblem reads: for a given $(\mathbf{u}^{n+\frac{1}{2}}, \boldsymbol{\eta}^{n+\frac{1}{2}}, \boldsymbol{v}^{n+\frac{1}{2}}, \mathbf{d}^{n+\frac{1}{2}}, \mathbf{w}^{n+\frac{1}{2}}, \mathbf{k}^{n+\frac{1}{2}}, \mathbf{z}^{n+\frac{1}{2}})$, find $(\mathbf{u}, \boldsymbol{\eta}, \boldsymbol{v}, \mathbf{d}, \mathbf{w}, \mathbf{k}, \mathbf{z})$ such that:

$$\begin{cases} \rho_F \partial_t \mathbf{u} = \nabla \cdot \boldsymbol{\sigma}, & \text{in} \quad (t_n, t_{n+1}) \times \Omega, \\ \nabla \cdot \mathbf{u} = 0, & \text{in} \quad (t_n, t_{n+1}) \times \Omega, \end{cases}$$

$$\begin{cases} \rho_K h \partial_t \boldsymbol{v} R = -J(\boldsymbol{\sigma} \circ \boldsymbol{\varphi})(\mathbf{n} \circ \boldsymbol{\varphi}), & \text{in} \quad (t_n, t_{n+1}) \times \omega, \\ \mathbf{u}|_\Gamma \circ \boldsymbol{\varphi} = \boldsymbol{v}, & \text{in} \quad (t_n, t_{n+1}) \times \omega, \end{cases}$$

$$\begin{cases} p = P_{\text{in/out}}(t), & \text{on} \quad \Gamma_{\text{in/out}}, \\ \mathbf{u} \times \mathbf{e}_z = 0, & \text{on} \quad \Gamma_{\text{in/out}}, \end{cases}$$

$$\begin{cases} \partial_t \boldsymbol{\eta} = 0, & \text{in} \quad (t_n, t_{n+1}) \times \omega, \\ \partial_t \mathbf{d}_i = 0, & \text{in} \quad (t_n, t_{n+1}) \times (0, l_i), \quad i = 1, \dots, n_E, \\ \partial_t \mathbf{w}_i = 0, & \text{in} \quad (t_n, t_{n+1}) \times (0, l_i), \quad i = 1, \dots, n_E, \end{cases}$$

$$\begin{cases} \partial_t \mathbf{k}_i = 0, & \text{in} \quad (t_n, t_{n+1}) \times (0, l_i), \quad i = 1, \dots, n_E, \\ \partial_t \mathbf{z}_i = 0, & \text{in} \quad (t_n, t_{n+1}) \times (0, l_i), \quad i = 1, \dots, n_E, \end{cases}$$

with initial data:

$$\begin{cases} \mathbf{u}(t_n) = \mathbf{u}^{n+1/2}, \boldsymbol{\eta}(t_n) = \boldsymbol{\eta}^{n+1/2}, \boldsymbol{v}(t_n) = \boldsymbol{v}^{n+1/2}, \mathbf{d}(t_n) = \mathbf{d}^{n+1/2}, \\ \mathbf{w}(t_n) = \mathbf{w}^{n+1/2}, \mathbf{k}(t_n) = \mathbf{k}^{n+1/2}, \mathbf{z}(t_n) = \mathbf{z}^{n+1/2}. \end{cases}$$

Then set $\mathbf{u}^{n+1} = \mathbf{u}(t_{n+1}), \boldsymbol{\eta}^{n+1} = \boldsymbol{\eta}(t_{n+1}), \boldsymbol{v}^{n+1} = \boldsymbol{v}(t_{n+1}), \mathbf{d}^{n+1} = \mathbf{d}(t_{n+1})$, $\mathbf{w}^{n+1} = \mathbf{w}(t_{n+1}), \mathbf{k}^{n+1} = \mathbf{k}(t_{n+1}), \mathbf{z}^{n+1} = \mathbf{z}(t_{n+1})$.

Crucial for a design of a stable scheme is the inclusion of structure inertia into the fluid subproblem, which guarantees energy balance at the time-discrete level, thereby avoiding stability problems due to the so-called *added mass effect*. Added mass effect is used to describe the elastodynamics of structures interacting with fluids with comparable densities, for which there is a significant exchange of energy between the fluid and structure motion, potentially causing instabilities is schemes that do not approximate well the energy exchange that occurs at the continuous level. Here, we emphasize that there is no added mass effect associated with the stent since the fluid velocity does not have the trace defined on the $1D$ set describing the stent, and therefore it is enough to include only the shell inertia into the fluid subproblem.

5. Existence of weak solutions

5.1. Function spaces

Motivated by the energy inequality (19), we define the following evolution spaces associated with the fluid problem, the Koiter shell problem, the mesh problem and the coupled mesh–shell problem:

- $V_F(0,T) = L^\infty(0,T;L^2(\Omega)) \cap L^2(0,T;V_F)$, where V_F is defined by (2),
- $V_K(0,T) = W^{1,\infty}(0,T;L^2(R;\omega)) \cap L^\infty(0,T;V_K)$, where V_K is defined by (4),
- $V_S(0,T) = W^{1,\infty}(0,T;L^2(\mathcal{N})) \cap L^\infty(0,T;V_S)$, where V_S is defined by (8),

- $V_{KS}(0,T) = \{(\boldsymbol{\eta}, \mathbf{d}, \mathbf{w}) \in V_K(0,T) \times V_S(0,T) : \boldsymbol{\eta} \circ \boldsymbol{\pi} = \mathbf{d} \text{ on } \prod_{i=1}^{n_E}(0, l_i)\}$.

The solution space for the coupled fluid–mesh–shell interaction problem involves the kinematic coupling condition, which is, thus, enforced in a strong way:

$$V(0,T) = \{(\mathbf{u}, \boldsymbol{\eta}, \mathbf{d}, \mathbf{w}) \in V_F(0,T) \times V_{KS}(0,T) : \mathbf{u} \circ \boldsymbol{\varphi} = \partial_t \boldsymbol{\eta} \text{ on } \omega\}.$$

The associated test space is given by:

$$Q(0,T) = \{(\boldsymbol{\upsilon}, \boldsymbol{\psi}, \boldsymbol{\xi}, \boldsymbol{\zeta}) \in C_c^1([0,T); V_F \times V_{KS}) : \boldsymbol{\upsilon} \circ \boldsymbol{\varphi} = \boldsymbol{\psi} \text{ on } \omega\}.$$

5.2. Definition of a weak solution

We are now in a position to state a definition of weak solutions of our fluid–mesh–shell interaction problem, with the fluid flow in Ω.

Definition 5.1. We say that $(\mathbf{u}, \boldsymbol{\eta}, \mathbf{d}, \mathbf{w}) \in V(0,T)$ is a weak solution of Problem 1 if for all test functions $(\boldsymbol{\upsilon}, \boldsymbol{\psi}, \boldsymbol{\xi}, \boldsymbol{\zeta}) \in Q(0,T)$ the following equality holds:

$$\begin{aligned}
&- \rho_F \int_0^T \int_\Omega \mathbf{u} \cdot \partial_t \boldsymbol{\upsilon} + 2\mu_F \int_0^T \int_\Omega \mathbf{D}(\mathbf{u}) : \mathbf{D}(\boldsymbol{\upsilon}) - \rho_K h \int_0^T \int_\omega \partial_t \boldsymbol{\eta} \cdot \partial_t \boldsymbol{\psi} R \\
&+ \int_0^T a_K(\boldsymbol{\eta}, \boldsymbol{\psi}) - \rho_S \sum_{i=1}^{n_E} A_i \int_0^T \int_0^{l_i} \partial_t \mathbf{d}_i \cdot \partial_t \boldsymbol{\xi}_i - \rho_S \sum_{i=1}^{n_E} \int_0^T \int_0^{l_i} M_i \partial_t \mathbf{w}_i \cdot \partial_t \boldsymbol{\zeta}_i \\
&+ \int_0^T a_S(\mathbf{w}, \boldsymbol{\zeta}) = \int_0^T \langle F(t), \boldsymbol{\upsilon} \rangle_{\Gamma_{\text{in/out}}} + \rho_F \int_\Omega \mathbf{u}_0 \cdot \boldsymbol{\upsilon}(0) + \rho_K h \int_\omega \boldsymbol{\upsilon}_0 \cdot \boldsymbol{\psi}(0) R \\
&+ \rho_S \sum_{i=1}^{n_E} A_i \int_0^{l_i} \mathbf{k}_{0i} \cdot \boldsymbol{\xi}_i(0) + \rho_S \sum_{i=1}^{n_E} \int_0^{l_i} M_i \mathbf{z}_{0i} \cdot \boldsymbol{\zeta}_i(0),
\end{aligned}$$

where

$$a_K(\boldsymbol{\eta}, \boldsymbol{\psi}) = \langle \mathcal{L}\boldsymbol{\eta}, \boldsymbol{\psi} \rangle,$$

$$a_S(\mathbf{w}, \boldsymbol{\zeta}) = \sum_{i=1}^{n_E} \int_0^{l_i} Q_i H_i Q_i^T \partial_s \mathbf{w}_i \cdot \partial_s \boldsymbol{\zeta}_i,$$

and

$$\langle F(t), \boldsymbol{\upsilon} \rangle_{\Gamma_{\text{in/out}}} = P_{\text{in}}(t) \int_{\Gamma_{\text{in}}} \upsilon_z - P_{\text{out}}(t) \int_{\Gamma_{\text{out}}} \upsilon_z.$$

5.3. Statement of main existence result

Our goal is to prove the existence of such weak solutions. More precisely, we prove the following main result of this manuscript:

Theorem 5.1. *Let* $\mathbf{u}_0 \in L^2(\Omega)$, $\boldsymbol{\eta}_0 \in H^1(\omega)$, $\boldsymbol{v}_0 \in L^2(R;\omega)$, $(\mathbf{d}_0, \mathbf{w}_0) \in V_S$, $(\mathbf{k}_0, \mathbf{z}_0) \in L^2(\mathcal{N};\mathbb{R}^6)$ *be such that*

$$\nabla \cdot \mathbf{u}_0 = 0,\ (\mathbf{u}_0|_\Gamma \circ \boldsymbol{\varphi}) \cdot \mathbf{e}_r = (\boldsymbol{v}_0)_r,\ \mathbf{u}_0|_{\Gamma_{\text{in/out}}} \times \mathbf{e}_z = 0,\ \boldsymbol{\eta}_0 \circ \boldsymbol{\pi} = \mathbf{d}_0.$$

Furthermore, let all the physical constants be positive: $\rho_K, \rho_S, \rho_F, \lambda, \mu, \mu_F > 0$ *and* $A_i > 0, \forall i = 1, \dots, n_E$, *and let* $P_{\text{in/out}} \in L^2_{loc}(0,\infty)$. *Then, for every* $T > 0$, *there exists a weak solution to Problem 1 in the sense of Definition 5.1.*

The rest of the manuscript is dedicated to designing a constructive proof of this existence result.

6. Approximate solutions

We construct approximate solutions to Problem 1 by semi-discretizing the subproblems defined in Sect. 4 using the Backward Euler scheme. Let $\Delta t = T/N$ be the time-discretization parameter so that the time interval $(0,T)$ is subdivided into N subintervals of width Δt. We define the vector of unknown approximate solutions

$$\mathbf{X}_N^{n+i/2} = (\mathbf{u}_N^{n+i/2}, \boldsymbol{\eta}_N^{n+i/2}, \boldsymbol{v}_N^{n+i/2}, \mathbf{d}_N^{n+i/2}, \mathbf{w}_N^{n+i/2}, \mathbf{k}_N^{n+i/2}, \mathbf{z}_N^{n+i/2}),$$

$n = 0, 1, \dots, N, i = 1, 2$, where $i = 1, 2$ denotes the solution of the structure and the fluid subproblem, respectively. We semi-discretize the problem so that the discrete version of the energy inequality (19) is preserved at every time step. We define the semi-discrete versions of the kinetic and elastic energy, and of dissipation, by the following:

$$\begin{aligned} E_N^{n+i/2} = {} & \rho_F \int_\Omega |\mathbf{u}^{n+i/2}|^2 + \rho_K h \int_\omega |\boldsymbol{v}^{n+i/2}|^2 R + a_K(\boldsymbol{\eta}^{n+i/2}, \boldsymbol{\eta}^{n+i/2}) \\ & + \rho_S \textstyle\sum_{i=1}^{n_E} A_i \int_0^{l_i} |\mathbf{k}_i^{n+i/2}|^2 + \rho_S \sum_{i=1}^{n_E} \int_0^{l_i} M_i |\mathbf{z}_i^{n+i/2}|^2 \\ & + a_S(\mathbf{w}^{n+i/2}, \mathbf{w}^{n+i/2}), \end{aligned} \tag{24}$$

$$D_N^{n+1} = 4\Delta t \mu_F \textstyle\int_\Omega |\mathbf{D}(\mathbf{u}^{n+1})|^2, \quad n = 0, \dots, N-1, \quad i = 1, 2. \tag{25}$$

6.1. The semi-discretized structure subproblem

In this step, $\mathbf{u}$ does not change, so

$$\mathbf{u}^{n+1/2} = \mathbf{u}^n.$$

Furthermore, we define $(\boldsymbol{\eta}^{n+1/2}, \boldsymbol{v}^{n+1/2}, \mathbf{d}^{n+1/2}, \mathbf{w}^{n+1/2}, \mathbf{k}^{n+1/2}, \mathbf{z}^{n+1/2})$ as the solution of the following problem, written in weak form:

$$\begin{aligned} \rho_K h \int_\omega \frac{\boldsymbol{v}^{n+1/2} - \boldsymbol{v}^n}{\Delta t} \cdot \boldsymbol{\psi} R + a_K(\boldsymbol{\eta}^{n+1/2}, \boldsymbol{\psi}) + \rho_S \sum_{i=1}^{n_E} A_i \int_0^{l_i} \frac{\mathbf{k}_i^{n+1/2} - \mathbf{k}_i^n}{\Delta t} \cdot \boldsymbol{\xi}_i \\ + \rho_S \sum_{i=1}^{n_E} \int_0^{l_i} M_i \frac{\mathbf{z}_i^{n+1/2} - \mathbf{z}_i^n}{\Delta t} \cdot \boldsymbol{\zeta}_i + a_S(\mathbf{w}^{n+1/2}, \boldsymbol{\zeta}) = 0, \end{aligned} \tag{26}$$

$$\left.\begin{aligned}
&\int_\omega \frac{\boldsymbol{\eta}^{n+1/2}-\boldsymbol{\eta}^n}{\Delta t}\cdot\boldsymbol{\psi}R = \int_\omega \boldsymbol{v}^{n+1/2}\cdot\boldsymbol{\psi}R,\\
&\int_0^{l_i} \frac{\mathbf{d}_i^{n+1/2}-\mathbf{d}_i^n}{\Delta t}\cdot\boldsymbol{\xi}_i = \int_0^{l_i}\mathbf{k}_i^{n+1/2}\cdot\boldsymbol{\xi}_i,\\
&\int_0^{l_i} \frac{\mathbf{w}_i^{n+1/2}-\mathbf{w}_i^n}{\Delta t}\cdot\boldsymbol{\zeta}_i = \int_0^{l_i}\mathbf{z}_i^{n+1/2}\cdot\boldsymbol{\zeta}_i,
\end{aligned}\right\}\ i=1,\dots,n_E,$$

for all test functions $(\boldsymbol{\psi},\boldsymbol{\xi},\boldsymbol{\zeta})\in V_{KS}$, where the solution space is defined by:

$$\begin{aligned}V_S^{\Delta t} := \{(\boldsymbol{\eta},\boldsymbol{v},\mathbf{d},\mathbf{w},\mathbf{k},\mathbf{z})\in V_K\times L^2(R;\omega)\times V_S\times L^2(\mathcal{N})\times L^2(\mathcal{N}):\\ \boldsymbol{\eta}\circ\boldsymbol{\pi}=\mathbf{d}\text{ on }\prod_{i=1}^{n_E}(0,l_i)\}.\end{aligned}\tag{27}$$

Proposition 6.1. *For each fixed $\Delta t>0$, the structure subproblem has a unique solution $(\boldsymbol{\eta}^{n+1/2},\boldsymbol{v}^{n+1/2},\mathbf{d}^{n+1/2},\mathbf{w}^{n+1/2},\mathbf{k}^{n+1/2},\mathbf{z}^{n+1/2})\in V_S^{\Delta t}$.*

Proof. The proof is a direct consequence of the Lax–Milgram lemma. To show this, we define a bilinear form on the mesh–shell space by replacing $\boldsymbol{v}^{n+1/2}$ by $\frac{\boldsymbol{\eta}^{n+1/2}-\boldsymbol{\eta}^n}{\Delta t}$, $\mathbf{k}_i^{n+1/2}$ by $\frac{\mathbf{d}_i^{n+1/2}-\mathbf{d}_i^n}{\Delta t}$ and $\mathbf{z}_i^{n+1/2}$ by $\frac{\mathbf{w}_i^{n+1/2}-\mathbf{w}_i^n}{\Delta t}$, for $i=1,\dots,n_E$, in the first equation in (26). We obtain

$$\begin{aligned}
&\rho_K h\int_\omega \frac{\boldsymbol{\eta}^{n+1/2}-\boldsymbol{\eta}^n}{(\Delta t)^2}\cdot\boldsymbol{\psi}R + a_K(\boldsymbol{\eta}^{n+1/2},\boldsymbol{\psi}) + \rho_S\sum_{i=1}^{n_E}A_i\int_0^{l_i}\frac{\mathbf{d}_i^{n+1/2}-\mathbf{d}_i^n}{(\Delta t)^2}\cdot\boldsymbol{\xi}_i\\
&\quad+\rho_S\sum_{i=1}^{n_E}\int_0^{l_i}M_i\frac{\mathbf{w}_i^{n+1/2}-\mathbf{w}_i^n}{(\Delta t)^2}\cdot\boldsymbol{\zeta}_i + a_S(\mathbf{w}^{n+1/2},\boldsymbol{\zeta})\\
&=\rho_K h\int_\omega\frac{\boldsymbol{v}^n}{\Delta t}\cdot\boldsymbol{\psi}R+\rho_S\sum_{i=1}^{n_E}A_i\int_0^{l_i}\frac{\mathbf{k}_i^n}{\Delta t}\cdot\boldsymbol{\xi}_i+\rho_S\sum_{i=1}^{n_E}\int_0^{l_i}M_i\frac{\mathbf{z}_i^n}{\Delta t}\cdot\boldsymbol{\zeta}_i.
\end{aligned}$$

We multiply this equality by $(\Delta t)^2$ and move all the terms from the n-th step to the right-hand side to obtain:

$$\begin{aligned}
&\rho_K h\int_\omega\boldsymbol{\eta}^{n+1/2}\cdot\boldsymbol{\psi}R+(\Delta t)^2a_K(\boldsymbol{\eta}^{n+1/2},\boldsymbol{\psi})+\rho_S\sum_{i=1}^{n_E}A_i\int_0^{l_i}\mathbf{d}_i^{n+1/2}\cdot\boldsymbol{\xi}_i\\
&+\rho_S\sum_{i=1}^{n_E}\int_0^{l_i}M_i\mathbf{w}_i^{n+1/2}\cdot\boldsymbol{\zeta}_i+(\Delta t)^2a_S(\mathbf{w}^{n+1/2},\boldsymbol{\zeta})=\rho_K h\int_\omega\Big(\boldsymbol{\eta}^n+\Delta t\boldsymbol{v}^n\Big)\cdot\boldsymbol{\psi}R\\
&+\rho_S\sum_{i=1}^{n_E}A_i\int_0^{l_i}\Big(\mathbf{d}_i^n+\Delta t\mathbf{k}_i^n\Big)\cdot\boldsymbol{\xi}_i+\rho_S\sum_{i=1}^{n_E}\int_0^{l_i}M_i\Big(\mathbf{w}_i^n+\Delta t\mathbf{z}_i^n\Big)\cdot\boldsymbol{\zeta}_i.
\end{aligned}$$

The left-hand side of the above equation defines the following bilinear form associated with the structure subproblem:

$$a((\boldsymbol{\eta},\mathbf{d},\mathbf{w}),(\boldsymbol{\psi},\boldsymbol{\xi},\boldsymbol{\zeta})) := \rho_K h \int_\omega \boldsymbol{\eta}\cdot\boldsymbol{\psi} R + (\Delta t)^2 a_K(\boldsymbol{\eta},\boldsymbol{\psi}) + \rho_S \sum_{i=1}^{n_E} A_i \int_0^{l_i} \mathbf{d}_i\cdot\boldsymbol{\xi}_i + \rho_S \sum_{i=1}^{n_E} \int_0^{l_i} M_i \mathbf{w}_i\cdot\boldsymbol{\zeta}_i + (\Delta t)^2 a_S(\mathbf{w},\boldsymbol{\zeta}). \tag{28}$$

In order to apply the Lax–Milgram lemma, we need to prove the continuity and coercivity of the bilinear form (28) on V_{KS}. To show that a is coercive, we write

$$\begin{aligned}
&a((\boldsymbol{\eta},\mathbf{d},\mathbf{w}),(\boldsymbol{\eta},\mathbf{d},\mathbf{w}))\\
&= \rho_K h \int_\omega |\boldsymbol{\eta}|^2 R + (\Delta t)^2 a_K(\boldsymbol{\eta},\boldsymbol{\eta}) + \rho_S \sum_{i=1}^{n_E} A_i \int_0^{l_i} |\mathbf{d}_i|^2\\
&\quad + \rho_S \sum_{i=1}^{n_E} \int_0^{l_i} M_i |\mathbf{w}_i|^2 + (\Delta t)^2 a_S(\mathbf{w},\mathbf{w})\\
&\geq c\Big(\|\boldsymbol{\eta}\|^2_{L^2(R;\omega)} + \|\boldsymbol{\eta}\|^2_k + \|\mathbf{d}\|^2_{L^2(\mathcal{N})} + \|\mathbf{w}\|^2_{L^2(\mathcal{N})} + \|\partial_s \mathbf{w}\|^2_{L^2(\mathcal{N})}\Big)\\
&\geq c\Big(\|\boldsymbol{\eta}\|^2_k + \|\mathbf{d}\|^2_{L^2(\mathcal{N})} + \|\mathbf{w}\|^2_{H^1(\mathcal{N})}\Big).
\end{aligned}$$

Now, we use the condition of inextensibility and unshearability to get a bound on $\|\partial_s \mathbf{d}\|^2_{L^2(\mathcal{N})}$:

$$\|\partial_s \mathbf{d}\|_{L^2(\mathcal{N})} = \|-\mathbf{t}\times\mathbf{w}\|_{L^2(\mathcal{N})} \leq C\|\mathbf{w}\|_{L^2(\mathcal{N})}.$$

Notice how the L^2-norm of infinitesimal rotation of cross sections keeps control over the gradient of displacement of the middle line. This now provides coercivity, i.e.,

$$a((\boldsymbol{\eta},\mathbf{d},\mathbf{w}),(\boldsymbol{\eta},\mathbf{d},\mathbf{w})) \geq c\Big(\|\boldsymbol{\eta}\|^2_k + \|\mathbf{d}\|^2_{H^1(\mathcal{N})} + \|\mathbf{w}\|^2_{H^1(\mathcal{N})}\Big).$$

The Lax–Milgram lemma implies the existence of a unique solution of problem (26). □

Proposition 6.2. *For each fixed $\Delta t > 0$, the structure subproblem (26) satisfies the following discrete energy equality:*

$$\begin{aligned}
E_N^{n+1/2} &+ \rho_K h \|\boldsymbol{v}^{n+1/2} - \boldsymbol{v}^n\|^2_{L^2(R;\omega)} + a_K(\boldsymbol{\eta}^{n+1/2} - \boldsymbol{\eta}^n, \boldsymbol{\eta}^{n+1/2} - \boldsymbol{\eta}^n)\\
&+ \rho_S \|\mathbf{k}^{n+1/2} - \mathbf{k}^n\|^2_a + \rho_S \|\mathbf{z}^{n+1/2} - \mathbf{z}^n\|^2_m\\
&+ a_S(\mathbf{w}^{n+1/2} - \mathbf{w}^n, \mathbf{w}^{n+1/2} - \mathbf{w}^n) = E_N^n,
\end{aligned} \tag{29}$$

where

$$\|\mathbf{k}\|^2_a := \sum_{i=1}^{n_E} A_i \|\mathbf{k}_i\|_{L^2(0,l_i)}.$$

Proof. We take $(\boldsymbol{v}^{n+1/2}, \mathbf{k}^{n+1/2}, \mathbf{z}^{n+1/2})$ as a test function in the first equation in (26), and replace them with the corresponding expressions: $(\boldsymbol{\eta}^{n+1/2} - \boldsymbol{\eta}^n)/\Delta t$ and $(\mathbf{w}^{n+1/2} - \mathbf{w}^n)/\Delta t$ in the bilinear forms a_S and a_K, respectively, to obtain:

$$\frac{\rho_K h}{\Delta t} \int_\omega (\boldsymbol{v}^{n+1/2} - \boldsymbol{v}^n)\cdot \boldsymbol{v}^{n+1/2} R + \frac{1}{\Delta t} a_K(\boldsymbol{\eta}^{n+1/2}, \boldsymbol{\eta}^{n+1/2} - \boldsymbol{\eta}^n)$$

$$+\frac{\rho_S}{\Delta t}\sum_{i=1}^{n_E} A_i \int_0^{l_i} (\mathbf{k}_i^{n+1/2}-\mathbf{k}_i^n)\cdot \mathbf{k}_i^{n+1/2} + \frac{\rho_S}{\Delta t}\sum_{i=1}^{n_E}\int_0^{l_i} M_i(\mathbf{z}_i^{n+1/2}-\mathbf{z}_i^n)\cdot \mathbf{z}_i^{n+1/2}$$
$$+\frac{1}{\Delta t}a_S(\mathbf{w}^{n+1/2},\mathbf{w}^{n+1/2}-\mathbf{w}^n)=0.$$

We then use the algebraic identity $(a-b)\cdot a=\frac{1}{2}(|a|^2+|a-b|^2-|b|^2)$ to deal with the mixed products. After multiplying the entire equation by $2\Delta t$, the first equation in (26) can be written as:

$$\rho_K h(\|\boldsymbol{\upsilon}^{n+1/2}\|^2+\|\boldsymbol{\upsilon}^{n+1/2}-\boldsymbol{\upsilon}^n\|^2)+a_K(\boldsymbol{\eta}^{n+1/2},\boldsymbol{\eta}^{n+1/2})+$$
$$a_K(\boldsymbol{\eta}^{n+1/2}-\boldsymbol{\eta}^n,\boldsymbol{\eta}^{n+1/2}-\boldsymbol{\eta}^n)+\rho_S(\|\mathbf{k}^{n+1/2}\|_a^2+\|\mathbf{k}^{n+1/2}-\mathbf{k}^n\|_a^2)+$$
$$\rho_S(\|\mathbf{z}^{n+1/2}\|_m^2+\|\mathbf{z}^{n+1/2}-\mathbf{z}^n\|_m^2)+a_S(\mathbf{w}^{n+1/2},\mathbf{w}^{n+1/2})+a_S(\mathbf{w}^{n+1/2}-\mathbf{w}^n,$$
$$\mathbf{w}^{n+1/2}-\mathbf{w}^n)=\rho_K h\|\boldsymbol{\upsilon}^n\|^2+a_K(\boldsymbol{\eta}^n,\boldsymbol{\eta}^n)+\rho_S\|\mathbf{k}^n\|_a^2+\rho_S\|\mathbf{z}^n\|_m^2+a_S(\mathbf{w}^n,\mathbf{w}^n).$$

Recall that $\mathbf{u}^{n+1/2}=\mathbf{u}^n$ in this subproblem, so we can add $\rho_F\|\mathbf{u}^{n+1/2}\|^2$ on the left-hand side, and $\rho_F\|\mathbf{u}^n\|^2$ on the right-hand side of the equation, to obtain exactly the energy equality (29). □

6.2. The semi-discretized fluid subproblem

In this step, the shell displacement $\boldsymbol{\eta}$, the mesh displacement $\mathbf{d}$, and the infinitesimal rotation $\mathbf{w}$ do not change, thus:

$$\boldsymbol{\eta}^{n+1}=\boldsymbol{\eta}^{n+1/2},\quad \mathbf{d}^{n+1}=\mathbf{d}^{n+1/2},\quad \mathbf{w}^{n+1}=\mathbf{w}^{n+1/2}.$$

Furthermore, the velocity of the mesh displacement and of the infinitesimal rotation has to be zero:

$$\mathbf{k}^{n+1}=\mathbf{k}^{n+1/2},\quad \mathbf{z}^{n+1}=\mathbf{z}^{n+1/2}.$$

A weak solution of the semi-discretized fluid subproblem is defined to be a function $(\mathbf{u}^{n+1},\boldsymbol{\upsilon}^{n+1})$ satisfying:

$$\begin{aligned}&\rho_F\int_\Omega \frac{\mathbf{u}^{n+1}-\mathbf{u}^n}{\Delta t}\cdot\boldsymbol{\upsilon}+2\mu_F\int_\Omega \mathbf{D}(\mathbf{u}^{n+1}):\mathbf{D}(\boldsymbol{\upsilon})\\ &+\rho_K h\int_\omega \frac{\boldsymbol{\upsilon}^{n+1}-\boldsymbol{\upsilon}^{n+1/2}}{\Delta t}\cdot\boldsymbol{\psi}R=\int_{\Gamma_{\text{in}}} P_{\text{in}}^n\upsilon_z-\int_{\Gamma_{\text{out}}} P_{\text{out}}^n\upsilon_z,\end{aligned}\tag{30}$$

for all test functions $(\boldsymbol{\upsilon},\boldsymbol{\psi})\in V_F\times L^2(R;\omega)$ such that $\boldsymbol{\upsilon}|_\Gamma\circ\boldsymbol{\varphi}=\boldsymbol{\psi}$ on ω, where the weak solution space is defined by:

$$V_F^{\Delta t}:=\{(\mathbf{u},\boldsymbol{\upsilon})\in V_F\times L^2(R;\omega):\mathbf{u}|_\Gamma\circ\boldsymbol{\varphi}=\boldsymbol{\upsilon}\text{ on }\omega\}.\tag{31}$$

Proposition 6.3. *For each fixed $\Delta t>0$, the fluid subproblem (30) has a unique solution $(\mathbf{u}^{n+1},\boldsymbol{\upsilon}^{n+1})\in V_F^{\Delta t}$.*

Proof. The proof is again a consequence of the Lax–Milgram lemma. We rewrite the first equation in (30) as follows:

$$\begin{aligned}&\frac{\rho_F}{\Delta t}\int_\Omega \mathbf{u}^{n+1}\cdot\boldsymbol{\upsilon}+2\mu_F\int_\Omega \mathbf{D}(\mathbf{u}^{n+1}):\mathbf{D}(\boldsymbol{\upsilon})+\rho_K h\int_\Omega \frac{\boldsymbol{\upsilon}^{n+1}}{\Delta t}\cdot\boldsymbol{\psi}R\\ &=\frac{\rho_F}{\Delta t}\int_\Omega \mathbf{u}^n\cdot\boldsymbol{\upsilon}+\frac{\rho_K h}{\Delta t}\int_\omega \boldsymbol{\upsilon}^{n+1/2}\cdot\boldsymbol{\psi}R+\int_{\Gamma_{\text{in}}} P_{\text{in}}^n\upsilon_z-\int_{\Gamma_{\text{out}}} P_{\text{out}}^n\upsilon_z.\end{aligned}$$

This defines the following bilinear form associated with problem (30):

$$a((\mathbf{u},\boldsymbol{v}),(\boldsymbol{v},\boldsymbol{\psi})) := \rho_F \int_\Omega \mathbf{u}\cdot\boldsymbol{v} + 2\Delta t\mu \int_\Omega \mathbf{D}(\mathbf{u}):\mathbf{D}(\boldsymbol{v}) + \rho_K h \int_\omega \boldsymbol{v}\cdot\boldsymbol{\psi} R. \tag{32}$$

We need to prove that this bilinear form a is coercive and continuous. In order to prove coercivity, we write:

$$\begin{aligned} a((\mathbf{u},\boldsymbol{v}),(\mathbf{u},\boldsymbol{v})) &= \rho_F \int_\Omega |\mathbf{u}|^2 + \Delta t 2\mu_F \int_\Omega |\mathbf{D}(\mathbf{u})|^2 + \rho_K h \int_\omega |\boldsymbol{v}|^2 R \\ &\geq c(\|\mathbf{u}\|^2_{L^2(\Omega)} + \|\mathbf{D}(\mathbf{u})\|^2_{L^2(\Omega)} + \|\boldsymbol{v}\|^2_{L^2(R;\omega)}) \\ &\geq c(\|\mathbf{u}\|^2_{H^1(\Omega)} + \|\boldsymbol{v}\|^2_{L^2(R;\omega)}). \end{aligned}$$

By applying Hölder inequality we get the continuity of a:

$$\begin{aligned} a((\mathbf{u},\boldsymbol{v}),(\boldsymbol{v},\boldsymbol{\psi})) \leq C\big(&\rho_F\|\mathbf{u}\|_{L^2(\Omega)}\|\boldsymbol{v}\|_{L^2(\Omega)} + \Delta t\mu_F\|\mathbf{u}\|_{H^1(\Omega)}\|\boldsymbol{v}\|_{H^1(\Omega)} \\ &+ \rho_K h\|\boldsymbol{v}\|_{L^2(R;\omega)}\|\boldsymbol{\psi}\|_{L^2(R;\omega)}\big). \end{aligned}$$

he Lax–Milgram lemma now implies the existence of a unique weak solution $(\mathbf{u}^{n+1},\boldsymbol{v}^{n+1})$ of the fluid subproblem (30). □

Proposition 6.4. *For each fixed $\Delta t > 0$, the solution of problem (30) satisfies the following discrete energy inequality:*

$$\begin{aligned} &E_N^{n+1} + \rho_F\|\mathbf{u}^{n+1}-\mathbf{u}^n\|^2_{L^2(\Omega)} + \rho_K h\|\boldsymbol{v}^{n+1}-\boldsymbol{v}^{n+1/2}\|^2_{L^2(R;\omega)} + D_N^{n+1} \\ &\qquad \leq E_N^{n+1/2} + C\Delta t((P_{\text{in}}^n)^2 + (P_{\text{out}}^n)^2), \end{aligned} \tag{33}$$

where $P^n_{\text{in/out}} = \frac{1}{\Delta t}\int_{n\Delta t}^{(n+1)\Delta t} P_{\text{in/out}}(t)\mathrm{d}t$.

Proof. We begin by replacing the test functions $(\boldsymbol{v},\boldsymbol{\psi})$ by $(\mathbf{u}^{n+1},\boldsymbol{v}^{n+1})$ in the weak formulation (30) to obtain:

$$\begin{aligned} &\frac{\rho_F}{\Delta t}\int_\Omega (\mathbf{u}^{n+1}-\mathbf{u}^n)\cdot\mathbf{u}^{n+1} + 2\mu_F\int_\Omega \mathbf{D}(\mathbf{u}^{n+1}):\mathbf{D}(\mathbf{u}^{n+1}) \\ &\quad + \frac{\rho_K h}{\Delta t}\int_\omega (\boldsymbol{v}^{n+1}-\boldsymbol{v}^{n+1/2})\cdot\boldsymbol{v}^{n+1}R = \int_{\Gamma_{\text{in}}} p^n u_z^{n+1} - \int_{\Gamma_{\text{out}}} p^n u_z^{n+1}. \end{aligned}$$

After applying the algebraic identity $(a-b)\cdot a = \frac{1}{2}(|a|^2 + |a-b|^2 - |b|^2)$ and multiplying the resulting equation by $2\Delta t$, we obtain:

$$\begin{aligned} &\rho_F(\|\mathbf{u}^{n+1}\|^2 + \|\mathbf{u}^{n+1}-\mathbf{u}^n\|^2) + 4\Delta t\mu\|\mathbf{D}(\mathbf{u}^{n+1})\|^2 \\ &\quad + \rho_K h(\|\boldsymbol{v}^{n+1}\|^2 + \|\boldsymbol{v}^{n+1}-\boldsymbol{v}^{n+1/2}\|^2) \\ &\leq \rho_F\|\mathbf{u}^n\|^2 + \rho_K h\|\boldsymbol{v}^{n+1/2}\|^2 + C\Delta t((P_{\text{in}}^n)^2 + (P_{\text{out}}^n)^2). \end{aligned}$$

Finally, recall that $\boldsymbol{\eta}^{n+1} = \boldsymbol{\eta}^{n+1/2}$ and $\mathbf{w}^{n+1} = \mathbf{w}^{n+1/2}$ in the fluid subproblem, so we can add $a_K(\boldsymbol{\eta}^{n+1},\boldsymbol{\eta}^{n+1})$ and $a_S(\mathbf{w}^{n+1},\mathbf{w}^{n+1})$ on the left-hand side, and $a_K(\boldsymbol{\eta}^{n+1/2},\boldsymbol{\eta}^{n+1/2})$ and $a_S(\mathbf{w}^{n+1/2},\mathbf{w}^{n+1/2})$ on the right-hand side. Furthermore, since $\mathbf{k}^{n+1} = \mathbf{k}^{n+1/2}$ and $\mathbf{z}^{n+1} = \mathbf{z}^{n+1/2}$, we add $\|\mathbf{k}^{n+1}\|^2_a$ and $\|\mathbf{z}^{n+1}\|^2_m$ on the left-hand side, and $\|\mathbf{k}^{n+1/2}\|^2_a$ and $\|\mathbf{z}^{n+1/2}\|^2_m$ on the right-hand side, to obtain exactly the energy inequality (33). □

6.3. Uniform energy estimates

Our goal is to ultimately show that there exists a subsequence of functions, parameterized by N (or Δt), defined by the time-discretization via Lie splitting specified above, which converges to a weak solution of Problem 1. To obtain this result, we start by showing that the sequence of approximations defined above, is uniformly bounded (uniformly with respect to Δt) in energy norm.

Lemma 6.1. *Let $\Delta t > 0$ and $N = T/\Delta t$. Furthermore, let $E_N^{n+1/2}, E_N^{n+1}$ and D_N^{n+1} be the kinetic energy and dissipation given by (24) and (25), respectively. Then, there exists a constant $K > 0$, independent of Δt (or N) such that the following estimates hold:*

1. $E_N^{n+1/2} \leq K, E_N^{n+1} \leq K, \forall n = 0, \ldots, N-1,$
2. $\sum_{n=0}^{N-1} D_N^{n+1} \leq K,$
3. $\sum_{n=0}^{N-1} \left(\rho_F \|\mathbf{u}^{n+1} - \mathbf{u}^n\|^2 + \rho_K h \|\boldsymbol{v}^{n+1} - \boldsymbol{v}^{n+1/2}\|^2 + \rho_K h \|\boldsymbol{v}^{n+1/2} - \boldsymbol{v}^n\|^2 \right) \leq K,$
4. $\sum_{n=0}^{N-1} \rho_S \left(\|\mathbf{k}^{n+1} - \mathbf{k}^n\|_a^2 + \|\mathbf{z}^{n+1} - \mathbf{z}^n\|_m^2 \right) \leq K,$
5. $\sum_{n=0}^{N-1} a_K(\boldsymbol{\eta}^{n+1} - \boldsymbol{\eta}^n, \boldsymbol{\eta}^{n+1} - \boldsymbol{\eta}^n) \leq K,$

   $\sum_{n=0}^{N-1} a_S(\mathbf{w}^{n+1} - \mathbf{w}^n, \mathbf{w}^{n+1} - \mathbf{w}^n) \leq K.$

Proof. We begin by adding the energy estimates (29) and (33) to obtain:

$$
\begin{aligned}
&E_N^{n+1/2} + \rho_K h \|\boldsymbol{v}^{n+1/2} - \boldsymbol{v}^n\|^2 + a_K(\boldsymbol{\eta}^{n+1/2} - \boldsymbol{\eta}^n, \boldsymbol{\eta}^{n+1/2} - \boldsymbol{\eta}^n) \\
&\quad + \rho_S \|\mathbf{k}^{n+1/2} - \mathbf{k}^n\|_a^2 + \rho_S \|\mathbf{z}^{n+1/2} - \mathbf{z}^n\|_m^2 \\
&\quad + a_S(\mathbf{w}^{n+1/2} - \mathbf{w}^n, \mathbf{w}^{n+1/2} - \mathbf{w}^n) + E_N^{n+1} + \rho_F \|\mathbf{u}^{n+1} - \mathbf{u}^n\|^2 \\
&\quad + \rho_K h \|\boldsymbol{v}^{n+1} - \boldsymbol{v}^{n+1/2}\|^2 + D_N^{n+1} \leq E_N^n + E_N^{n+1/2} + C\Delta t((P_{\text{in}}^n)^2 + (P_{\text{out}}^n)^2).
\end{aligned}
$$

We take the sum from $n = 0$ to $n = N-1$ on both sides to obtain:

$$
\begin{aligned}
&E_N^N + \sum_{n=0}^{N-1} D_N^{n+1} + \sum_{n=0}^{N-1} \Big(\rho_F \|\mathbf{u}^{n+1} - \mathbf{u}^n\|^2 + \rho_K h \|\boldsymbol{v}^{n+1} - \boldsymbol{v}^{n+1/2}\|^2 \\
&\quad + \rho_K h \|\boldsymbol{v}^{n+1/2} - \boldsymbol{v}^n\|^2 + \rho_S \|\mathbf{k}^{n+1/2} - \mathbf{k}^n\|_a^2 + \rho_S \|\mathbf{z}^{n+1/2} - \mathbf{z}^n\|_m^2 \\
&\quad + a_K(\boldsymbol{\eta}^{n+1/2} - \boldsymbol{\eta}^n, \boldsymbol{\eta}^{n+1/2} - \boldsymbol{\eta}^n) + a_S(\mathbf{w}^{n+1/2} - \mathbf{w}^n, \mathbf{w}^{n+1/2} - \mathbf{w}^n) \Big) \\
&\leq E_0 + C\Delta t \sum_{n=o}^{N-1} \left((P_{\text{in}}^n)^2 + (P_{\text{out}}^n)^2 \right).
\end{aligned}
$$

The term involving the inlet and outlet pressure data can be easily estimated by recalling that on each subinterval (t_n, t_{n+1}) the pressure data is approximated by a constant, which is equal to the average value of the pressure over that time interval. Therefore, after using Hölder inequality, we have:

$$
\Delta t \sum_{n=0}^{N-1} (P_{\text{in}}^n)^2 = \Delta t \sum_{n=0}^{N-1} \Big(\frac{1}{\Delta t} \int_{n\Delta t}^{(n+1)\Delta t} P_{\text{in}}(t) \mathrm{d}t \Big)^2 \leq \|P_{\text{in}}\|_{L^2(0,T)}^2. \tag{34}
$$

We can now bound the right-hand side in the above energy estimate by using the just calculated pressure estimate, to obtain all the statements in the Lemma, with the constant $K = E_0 + C \left(\|P_{\text{in}}\|_{L^2(0,T)}^2 + \|P_{\text{out}}\|_{L^2(0,T)}^2 \right)$. □

7. Convergence of approximate solutions

The approach described above defines a set of discrete values in time, which can be used to define approximate functions on $(0,T)$. Indeed, we define approximate solutions on $(0,T)$ to be the functions, which are piecewise constant on each subinterval $((n-1)\Delta t, n\Delta t],\ n=1,\dots,N$ of $(0,T)$:

- $\mathbf{u}_N(t,\cdot)=\mathbf{u}_N^n,\ \boldsymbol{\eta}_N(t,\cdot)=\boldsymbol{\eta}_N^n, \forall t\in((n-1)\Delta t, n\Delta t]$,
- $\boldsymbol{v}_N(t,\cdot)=\boldsymbol{v}_N^n,\ \hat{\boldsymbol{v}}_N(t,\cdot)=\boldsymbol{v}_N^{n-1/2}, \forall t\in((n-1)\Delta t, n\Delta t]$,
- $\mathbf{d}_N(t,\cdot)=\mathbf{d}_N^n,\ \mathbf{w}_N(t,\cdot)=\mathbf{w}_N^n, \forall t\in((n-1)\Delta t, n\Delta t]$,
- $\mathbf{k}_N(t,\cdot)=\mathbf{k}_N^n,\ \mathbf{z}_N(t,\cdot)=\mathbf{z}_N^n, \forall t\in((n-1)\Delta t, n\Delta t]$.

In the second bullet above, we used $\hat{\boldsymbol{v}}_N(t,\cdot)=\boldsymbol{v}_N^{n-1/2}$ to denote the approximate shell velocity functions determined by the structure subproblem, and $\boldsymbol{v}_N(t,\cdot)=\boldsymbol{v}_N^n$ to denote the approximate shell velocity functions determined by the fluid subproblem. We emphasize that these are not necessarily the same. As a consequence, the kinematic coupling condition, which involves the shell velocity, is asynchronously satisfied by this scheme at each time step. We will show, however, that the difference between these approximate sequences for the shell velocity converges to zero in L^2 as $\Delta t\to 0$.

7.1. Weak and weak* convergence

Using the energy estimates presented in Lemma 6.1, we will show that the approximate sequences of functions defined above for all $t\in(0,T)$, are uniformly bounded in the appropriate solution spaces involving both space and time. This will provide weakly and weakly* convergent subsequences of approximate functions, for which we will show convergence to a weak solution of the coupled, continuous problem, as $\Delta t\to 0$.

Proposition 7.1. *The sequence $(\mathbf{u}_N)_{N\in\mathbb{N}}$ is uniformly bounded in $L^\infty(0,T;L^2(\Omega))\cap L^2(0,T;H^1(\Omega))$.*

Proof. The uniform boundedness of $(\mathbf{u}_N)$ in $L^\infty(0,T;L^2(\Omega))$ follows directly from the first statement of Lemma 6.1. To show the uniform boundedness of $(\mathbf{u}_N)$ in $L^2(0,T;H^1(\Omega))$, notice that from the second statement of Lemma 6.1 we have:

$$\sum_{n=1}^{N}\int_\Omega |\mathbf{D}(\mathbf{u}_N^n)|^2\Delta t\le K, \tag{35}$$

where $\mathbf{D}(\mathbf{u}_N^n)$ is the symmetrized gradient. By applying Korn inequality, we obtain

$$\|\nabla\mathbf{u}_N^n\|^2_{L^2(\Omega)}\le C\|\mathbf{D}(\mathbf{u}_N^n)\|^2_{L^2(\Omega)}.$$

Taking the sum from $n=1,\dots,N$, we get the following estimate

$$\sum_{n=1}^{N}\|\nabla\mathbf{u}_N^n\|^2_{L^2(\Omega)}\Delta t\le C\sum_{n=1}^{N}\|\mathbf{D}(\mathbf{u}_N^n)\|^2_{L^2(\Omega)}\Delta t,$$

which implies that the sequence $(\nabla\mathbf{u}_N)$ is uniformly bounded in $L^2(0,T;L^2(\Omega))$, and so the sequence $(\mathbf{u}_N)$ is uniformly bounded in $L^2(0,T;H^1(\Omega))$. □

Proposition 7.2. *The sequence $(\boldsymbol{\eta}_N)_{N\in\mathbb{N}}$ is uniformly bounded in $L^\infty(0,T;V_K)$, and the sequence $(\mathbf{w}_N)_{N\in\mathbb{N}}$ is uniformly bounded in $L^\infty(0,T;H^1(\mathcal{N}))$.*

Proof. From Lemma 6.1, we have that $E_N^n\le K,\ \forall n=0,\dots,N-1$, which implies

$$\|\boldsymbol{\eta}_N(t)\|_k^2\le a_K(\boldsymbol{\eta}_N(t),\boldsymbol{\eta}_N(t))\le K,\quad \forall t\in[0,T].$$

Therefore,

$$\|\boldsymbol{\eta}_N\|_{L^\infty(0,T;V_K)} \leq K.$$

The boundedness of the sequence $(\mathbf{w}_N)_{N\in\mathbb{N}}$ also follows from the first statement of Lemma 6.1. Namely, we have

$$\|\mathbf{w}_N(t)\|^2_{L^2(\mathcal{N})} \leq \|\mathbf{w}_N(t)\|^2_m \leq K,$$
$$\|\partial_s \mathbf{w}_N(t)\|^2_{L^2(\mathcal{N})} \leq a_S(\mathbf{w}_N(t), \mathbf{w}_N(t)) \leq K,$$

which concludes the proof. □

The following uniform bounds for the shell and mesh approximate velocities are a direct consequence of Lemma 6.1.

Proposition 7.3. *The following uniform bounds for the shell and mesh approximate velocities hold:*

(i) $(\boldsymbol{v}_N)_{N\in\mathbb{N}}$ *is uniformly bounded in* $L^\infty(0,T;L^2(R;\omega))$,
$(\hat{\boldsymbol{v}}_N)_{N\in\mathbb{N}}$ *is uniformly bounded in* $L^\infty(0,T;L^2(R;\omega))$,
(ii) $(\mathbf{k}_N)_{N\in\mathbb{N}}$ *is uniformly bounded in* $L^\infty(0,T;L^2(\mathcal{N}))$,
$(\mathbf{z}_N)_{N\in\mathbb{N}}$ *is uniformly bounded in* $L^\infty(0,T;L^2(\mathcal{N}))$.

To pass to the limit in the weak formulation of approximate solutions, we need additional regularity in time of the sequences $(\boldsymbol{\eta}_N)_{N\in\mathbb{N}}$, $(\mathbf{d}_N)_{N\in\mathbb{N}}$ and $(\mathbf{w}_N)_{N\in\mathbb{N}}$. For this purpose, we introduce a slightly different set of approximate functions. Namely, for each fixed Δt, define $\tilde{\boldsymbol{\eta}}_N, \tilde{\mathbf{d}}_N$ and $\tilde{\mathbf{w}}_N$ to be continuous, *linear* on each subinterval $[(n-1)\Delta t, n\Delta t]$, $n = 1,\dots,N$, and such that

$$\begin{aligned}
&\tilde{\mathbf{u}}_N(n\Delta t,\cdot) = \mathbf{u}_N(n\Delta t,\cdot),\\
&\tilde{\boldsymbol{\eta}}_N(n\Delta t,\cdot) = \boldsymbol{\eta}_N(n\Delta t,\cdot), \tilde{\boldsymbol{v}}_N(n\Delta t,\cdot) = \boldsymbol{v}_N(n\Delta t,\cdot),\\
&\tilde{\mathbf{d}}_N(n\Delta t,\cdot) = \mathbf{d}_N(n\Delta t,\cdot), \tilde{\mathbf{w}}_N(n\Delta t,\cdot) = \mathbf{w}_N(n\Delta t,\cdot),\\
&\tilde{\mathbf{k}}_N(n\Delta t,\cdot) = \mathbf{k}_N(n\Delta t,\cdot), \tilde{\mathbf{z}}_N(n\Delta t,\cdot) = \mathbf{z}_N(n\Delta t,\cdot).
\end{aligned} \tag{36}$$

We now observe:

$$\partial_t \tilde{\boldsymbol{\eta}}_N(t) = \frac{\boldsymbol{\eta}_N^{n+1} - \boldsymbol{\eta}_N^n}{\Delta t} = \frac{\boldsymbol{\eta}_N^{n+1/2} - \boldsymbol{\eta}_N^n}{\Delta t} = \boldsymbol{v}_N^{n+1/2}, \quad t \in (n\Delta t, (n+1)\Delta t].$$

Since $\hat{\boldsymbol{v}}_N$ is a piecewise constant function, as defined before via $\hat{\boldsymbol{v}}_N(t,\cdot) = \boldsymbol{v}_N^{n+1/2}$, for $t \in (n\Delta t, (n+1)\Delta t]$, we see that

$$\partial_t \tilde{\boldsymbol{\eta}}_N = \hat{\boldsymbol{v}}_N \text{ a.e. on } (0,T). \tag{37}$$

From (37), and from the uniform boundedness of $E_N^{n+i/2}$ provided by Lemma 6.1, we obtain the uniform boundedness of $(\tilde{\boldsymbol{\eta}}_N)_{N\in\mathbb{N}}$ in $W^{1,\infty}(0,T;L^2(R;\omega))$. Now, since sequences $(\tilde{\boldsymbol{\eta}}_N)_{N\in\mathbb{N}}$ and $(\boldsymbol{\eta}_N)_{N\in\mathbb{N}}$ have the same limit (distributional limit is unique), we get that the weak* limit of $\boldsymbol{\eta}_N$ is, in fact, in $W^{1,\infty}(0,T;L^2(R;\omega))$.

Using analogous arguments, one also obtains that the weak* limits of $(\mathbf{d}_N)_{N\in\mathbb{N}}$ and $(\mathbf{w}_N)_{N\in\mathbb{N}}$ are in $W^{1,\infty}(0,T;L^2(\mathcal{N}))$. This is because the corresponding velocity approximations are uniformly bounded in the corresponding norms, as stated in part 4. of Lemma 6.1.

Notice that we do not get any bounds on the sequence $(\mathbf{d}_N)_{N\in\mathbb{N}}$ from the uniform energy estimates. Nevertheless, using the condition of inextensibility and unshearability, together with the regularity of $\mathbf{w}_N$, one can easily prove the H^1-regularity in space of $\mathbf{d}_N$. More precisely, the following result holds true:

Corollary 7.1. *The sequence* $(\mathbf{d}_N)_{N\in\mathbb{N}}$ *is uniformly bounded in* $L^\infty(0,T;H^1(\mathcal{N}))$.

From the uniform boundedness of approximate sequences, we can now conclude the following weak and weak* convergence results:

Lemma 7.1. *There exist subsequences* $(\mathbf{u}_N)_{N\in\mathbb{N}}, (\boldsymbol{\eta}_N)_{N\in\mathbb{N}}, (\boldsymbol{v}_N)_{N\in\mathbb{N}}, (\hat{\boldsymbol{v}}_N)_{N\in\mathbb{N}}$, $(\mathbf{d}_N)_{N\in\mathbb{N}}, (\mathbf{w}_N)_{N\in\mathbb{N}}, (\mathbf{k}_N)_{N\in\mathbb{N}}, (\mathbf{z}_N)_{N\in\mathbb{N}}$, *and the functions* $\mathbf{u}\in L^\infty(0,T;L^2(\Omega))\cap L^2(0,T;H^1(\Omega)), \boldsymbol{\eta}\in L^\infty(0,T;V_K)\cap W^{1,\infty}(0,T;L^2(R;\omega)), \mathbf{d},\mathbf{w}\in L^\infty(0,T;H^1(\mathcal{N}))\cap W^{1,\infty}(0,T;L^2(\mathcal{N})), \boldsymbol{v},\hat{\boldsymbol{v}}\in L^\infty(0,T;L^2(R;\omega))$, *and* $\mathbf{k},\mathbf{z}\in L^\infty(0,T;L^2(\mathcal{N}))$, *such that*

$$\begin{aligned}
&\mathbf{u}_N \rightharpoonup \mathbf{u} \text{ weakly* in } L^\infty(0,T;L^2(\Omega)),\\
&\mathbf{u}_N \rightharpoonup \mathbf{u} \text{ weakly in } L^2(0,T;H^1(\Omega)),\\
&\boldsymbol{\eta}_N \rightharpoonup \boldsymbol{\eta} \text{ weakly* in } L^\infty(0,T;V_K),\\
&\boldsymbol{\eta}_N \rightharpoonup \boldsymbol{\eta} \text{ weakly* in } W^{1,\infty}(0,T;L^2(R;\omega)),\\
&\mathbf{d}_N \rightharpoonup \mathbf{d} \text{ weakly* in } L^\infty(0,T;H^1(\mathcal{N})),\\
&\mathbf{d}_N \rightharpoonup \mathbf{d} \text{ weakly* in } W^{1,\infty}(0,T;L^2(\mathcal{N})),\\
&\mathbf{w}_N \rightharpoonup \mathbf{w} \text{ weakly* in } L^\infty(0,T;H^1(\mathcal{N})),\\
&\mathbf{w}_N \rightharpoonup \mathbf{w} \text{ weakly* in } W^{1,\infty}(0,T;L^2(\mathcal{N})),\\
&\boldsymbol{v}_N \rightharpoonup \boldsymbol{v} \text{ weakly* in } L^\infty(0,T;L^2(R;\omega)),\\
&\hat{\boldsymbol{v}}_N \rightharpoonup \hat{\boldsymbol{v}} \text{ weakly* in } L^\infty(0,T;L^2(R;\omega)),\\
&\mathbf{k}_N \rightharpoonup \mathbf{k} \text{ weakly* in } L^\infty(0,T;L^2(\mathcal{N})),\\
&\mathbf{z}_N \rightharpoonup \mathbf{z} \text{ weakly* in } L^\infty(0,T;L^2(\mathcal{N})).
\end{aligned}$$

Furthermore,

$$\boldsymbol{v}=\hat{\boldsymbol{v}}.$$

Proof. We only need to show that $\boldsymbol{v}=\hat{\boldsymbol{v}}$. To show this, we use the definition of approximate sequences as step functions in t, i.e.,

$$\begin{aligned}
\|\boldsymbol{v}_N-\hat{\boldsymbol{v}}_N\|^2_{L^2(0,T;L^2(R;\omega))} &= \int_0^T \|\boldsymbol{v}_N-\hat{\boldsymbol{v}}_N\|^2_{L^2(R;\omega)}dt = \sum_{n=0}^{N-1}\int_{t_n}^{t_{n+1}} \|\boldsymbol{v}_N^{n+1}-\boldsymbol{v}_N^{n+1/2}\|^2_{L^2(R;\omega)}\mathrm{d}t\\
&= \sum_{n=0}^{N-1}\|\boldsymbol{v}_N^{n+1}-\boldsymbol{v}_N^{n+1/2}\|^2_{L^2(R;\omega)}\Delta t. \le K\Delta t.
\end{aligned}$$

The last inequality follows from the third statement of Lemma 6.1. By letting $\Delta t\to 0$, we get that $\boldsymbol{v}=\hat{\boldsymbol{v}}$. □

7.2. Passing to the limit and proof of main result

We start by first writing the weak formulation of the coupled, semi-discretized problem. For this purpose, take $(\boldsymbol{\psi}(t),\boldsymbol{\xi}(t),\boldsymbol{\zeta}(t))$ as the test functions in the first equation in (26) and integrate with respect to t from $n\Delta t$ to $(n+1)\Delta t$. Then, take $(\boldsymbol{v}(t),\boldsymbol{\psi}(t))$ as the test functions in the first equation in (30) and again integrate over the same time interval. Add the two equations together to obtain

$$\rho_F\int_{n\Delta t}^{(n+1)\Delta t}\int_\Omega \frac{\mathbf{u}^{n+1}-\mathbf{u}^n}{\Delta t}\cdot\boldsymbol{v}+2\mu_F\int_{n\Delta t}^{(n+1)\Delta t}\int_\Omega \mathbf{D}(\mathbf{u}^{n+1}):\mathbf{D}(\boldsymbol{v})$$

$$+\rho_K h\int_{n\Delta t}^{(n+1)\Delta t}\int_{\omega}\frac{\boldsymbol{v}^{n+1}-\boldsymbol{v}^n}{\Delta t}\cdot\boldsymbol{\psi}R+\int_{n\Delta t}^{(n+1)\Delta t}a_K(\boldsymbol{\eta}^{n+1/2},\boldsymbol{\psi})$$
$$+\rho_S\int_{n\Delta t}^{(n+1)\Delta t}\sum_{i=1}^{n_E}A_i\int_0^{l_i}\frac{\mathbf{k}_i^{n+1/2}-\mathbf{k}_i^n}{\Delta t}\cdot\boldsymbol{\xi}_i+\rho_S\int_{n\Delta t}^{(n+1)\Delta t}\sum_{i=1}^{n_E}\int_0^{l_i}M_i\frac{\mathbf{z}_i^{n+1/2}-\mathbf{z}_i^n}{\Delta t}\cdot\boldsymbol{\zeta}_i$$
$$+\int_{n\Delta t}^{(n+1)\Delta t}a_S(\mathbf{w}^{n+1/2},\boldsymbol{\zeta})=\int_{n\Delta t}^{(n+1)\Delta t}\int_{\Gamma_{\text{in}}}p^n\upsilon_z-\int_{n\Delta t}^{(n+1)\Delta t}\int_{\Gamma_{\text{out}}}p^n\upsilon_z.$$

By using the definition of approximate solutions as functions of t, and by taking the sum from $n=0,\ldots,N-1$ to get the time integrals over $(0,T)$, we get:

$$\rho_F\int_0^T\int_\Omega\partial_t\tilde{\mathbf{u}}_N\cdot\boldsymbol{v}+2\mu_F\int_0^T\int_\Omega\mathbf{D}(\mathbf{u}_N):\mathbf{D}(\boldsymbol{v})$$
$$+\rho_K h\int_0^T\int_\omega\partial_t\tilde{\boldsymbol{v}}_N\cdot\boldsymbol{\psi}R+\int_0^T a_K(\boldsymbol{\eta}_N,\boldsymbol{\psi})$$
$$+\rho_S\int_0^T\sum_{i=1}^{n_E}A_i\int_0^{l_i}\partial_t(\tilde{\mathbf{k}}_N)_i\cdot\boldsymbol{\xi}_i+\rho_S\int_0^T\sum_{i=1}^{n_E}\int_0^{l_i}M_i\partial_t(\tilde{\mathbf{z}}_N)_i\cdot\boldsymbol{\zeta}_i$$
$$+\int_0^T a_S(\mathbf{w}_N,\boldsymbol{\zeta})=\int_0^T P_{\text{in}}^N\int_{\Gamma_{\text{in}}}\upsilon_z-\int_0^T P_{\text{out}}^N\int_{\Gamma_{\text{out}}}\upsilon_z.$$

Here, $\tilde{\mathbf{u}}_N,\tilde{\boldsymbol{v}}_N,\tilde{\mathbf{k}}_N$ and $\tilde{\mathbf{z}}_N$ are the piecewise linear functions defined in (36), while $\mathbf{u}_N,\boldsymbol{\eta}_N$ and $\mathbf{w}_N$ are piecewise constant functions. Integration by parts with respect to time gives:

$$-\rho_F\int_0^T\int_\Omega\tilde{\mathbf{u}}_N\cdot\partial_t\boldsymbol{v}+2\mu_F\int_0^T\int_\Omega\mathbf{D}(\mathbf{u}_N):\mathbf{D}(\boldsymbol{v})-\rho_K h\int_0^T\int_\omega\tilde{\boldsymbol{v}}_N\cdot\partial_t\boldsymbol{\psi}R$$
$$+\int_0^T a_K(\boldsymbol{\eta}_N,\boldsymbol{\psi})-\rho_S\int_0^T\sum_{i=1}^{n_E}A_i\int_0^{l_i}(\tilde{\mathbf{k}}_N)_i\cdot\partial_t\boldsymbol{\xi}_i$$
$$-\rho_S\int_0^T\sum_{i=1}^{n_E}\int_0^{l_i}M_i(\mathbf{z}_N)_i\cdot\partial_t\boldsymbol{\zeta}_i+\int_0^T a_S(\mathbf{w}_N,\boldsymbol{\zeta})=\int_0^T P_{\text{in}}^N\int_{\Gamma_{\text{in}}}\upsilon_z \tag{38}$$
$$-\int_0^T P_{\text{out}}^N\int_{\Gamma_{\text{out}}}\upsilon_z+\rho_F\int_\Omega\mathbf{u}_0\cdot\boldsymbol{v}(0)+\rho_K h\int_\omega\boldsymbol{v}_0\cdot\boldsymbol{\psi}(0)R$$
$$+\rho_S\sum_{i=1}^{n_E}A_i\int_0^{l_i}\mathbf{k}_{0i}\cdot\boldsymbol{\xi}_i(0)+\rho_S\sum_{i=1}^{n_E}\int_0^{l_i}M_i\mathbf{z}_{0i}\cdot\boldsymbol{\zeta}_i(0),$$

where we recall that

$$\nabla\cdot\mathbf{u}_N=0,\quad \mathbf{u}_N|_\Gamma\circ\varphi=\boldsymbol{v}_N,\quad \boldsymbol{\eta}_N\circ\boldsymbol{\pi}=\mathbf{d}_N.$$

Using the convergence results obtained for the approximate functions in Lemma 7.1, we can pass to the limit in all the terms. Thus, we have shown that the limiting functions satisfy the weak form of Problem 1 in the sense of Definition 5.1. This completes the proof of the main result of this manuscript, stated in Theorem 5.1.

8. Numerical examples

In this section, we present numerical simulations of the FSI problem studied above and compare our numerical results with the results of the FSI simulation in which stent is assumed to be a mesh-like structure, embedded in the 2D Koiter shell of thickness h, and modeled via jump discontinuities in the Koiter shell coefficients, as studied in [8]. The scheme we developed to solve the resulting FSI problem follows the Lie splitting strategy, used in the proof of existence of solutions, presented above.

8.1. The 1D stent model FSI

For the simulation of the fluid–shell–mesh interaction problem where the stent is modeled as a 1D hyperbolic mesh described above, we use a finite element method-based approach. The stent is simulated using the mixed formulation, described in [35], in which the inextensibility and unshearability of the curved rods are included in the function space (8). See [34] for details of the numerical scheme and for error estimates. These estimates hold in the finite element framework in which the finite elements used for Lagrange multipliers associated with the inextensibility and unshearability are of one order less than the order of the finite elements used for displacement and rotations.

The shell in our fluid–shell–mesh interaction simulations is assumed to be of Naghdi type. Naghdi shell is a small perturbation of the Koiter model with respect to the shell thickness [53]. The reason for the use of Naghdi shell instead of the Koiter shell is computational simplicity and efficiency. Koiter shell is fourth order in flexural displacements, which leads to the use of C^1 Hermite finite elements in the conformal approximation, instead of the Lagrangian elements which can be used for the simulation of the Naghdi shell model, which can be formulated within H^1, as shown in [53]. As a result, the coupling between the Naghdi shell and the 1D stent model is computationally easier and more natural than the Koiter shell-1D stent coupling, see [12]. The finite elements used for the shell model are P2 elements and the elements for the stent model are restrictions of the shell elements on the stent struts, i.e., P2 for displacements and rotations (and P1 for Lagrange multipliers) as suggested by the error estimates in [34]. The fluid is solved using P1b elements for the velocity and P1 for the pressure, see Fig. 2.

We study a benchmark problem consisting of a straight cylinder containing the fluid whose flow is driven by the time-dependent inlet and outlet normal stress data, as in [8] (see also [28]). At the inlet, the normal stress is a pressure pulse, while at the outlet the normal stress is set to zero:

$$\boldsymbol{\sigma n}|_{\Gamma_{\text{in}}} = -p_N \boldsymbol{n} = -\frac{P_{\max}}{2}\left[1-\cos\left(\frac{\pi t}{2.5}\right)\right]\boldsymbol{n}, \tag{39}$$

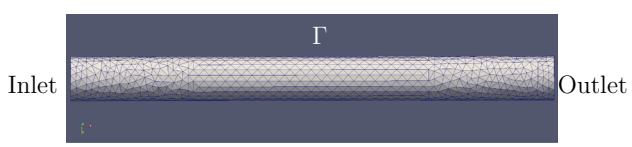

FIG. 2. Reference domain with an unstructured tetrahedron mesh. In the stented region, the mesh follows the 1D geometry of the stent, which cannot be explicitly seen, but can be compared to the 2D stent geometry in Fig. 8

TABLE 1. *Structure parameters for the elastic shell and 1D stent model*

Shell density	$\rho_a = 1100$ kg/m^3	Shell thickness	$h_a = 5.8 \times 10^{-4}$ m
Stent density	$\rho_s = 8500$ kg/m^3	Stent thickness	$h_s = 1.0 \times 10^{-4}$ m
Shell Poisson ratio	$\nu_a = 0.4$	Stent Poisson ratio	$\nu_s = 0.31$
Shell Young modulus	$E_a = 4 \times 10^5$ Pascal	Shell Shear modulus	$G_a = \frac{E_a}{2(1+\nu_a)} = 1.43 \times 10^5$ Pascal
Stent Young modulus	$E_s = 2.1 \times 10^{11}$ Pascal	Stent Shear modulus	$G_s = \frac{E_s}{2(1+\nu_s)} = 0.8 \times 10^{11}$ Pascal

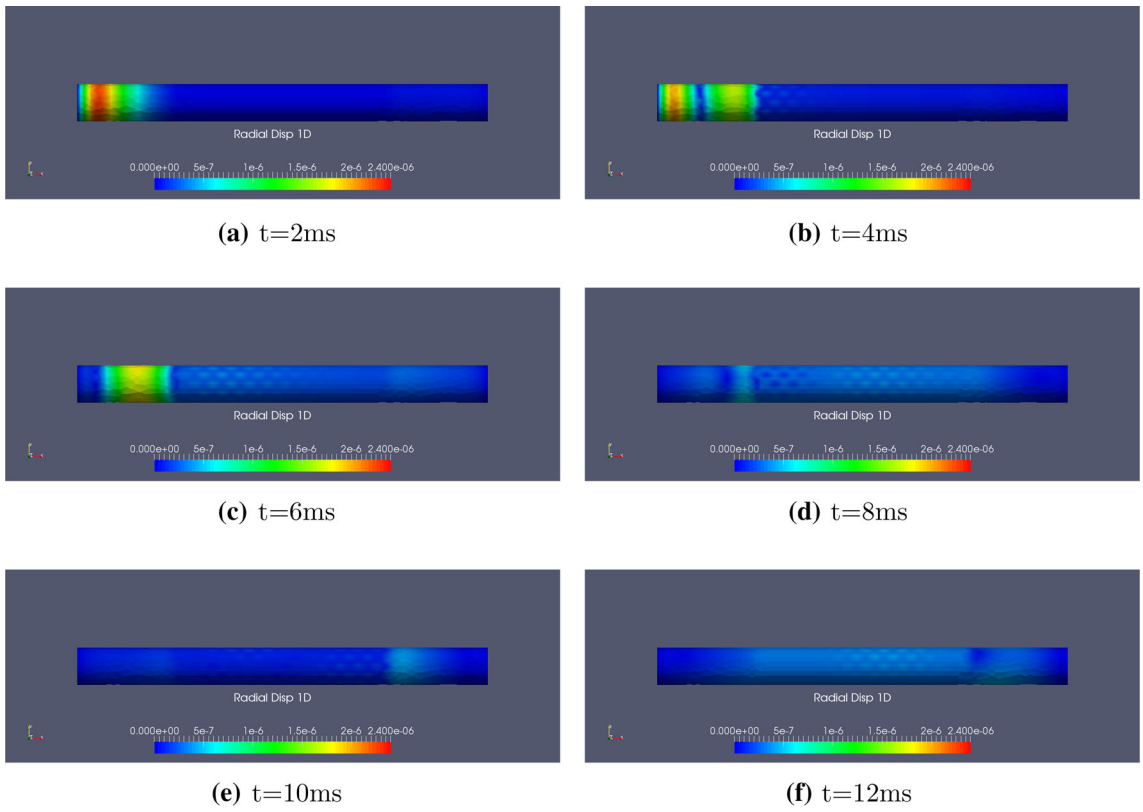

(a) t=2ms **(b)** t=4ms

(c) t=6ms **(d)** t=8ms

(e) t=10ms **(f)** t=12ms

FIG. 3. 1D stent FSI simulations: the snapshots of radial displacement at six different times ($t = 2$ ms, 4 ms, 6 ms, 8 ms, 10 ms and 12 ms)

$$\boldsymbol{\sigma n}|_{\Gamma_{\text{out}}} = -p_N \boldsymbol{n} = \mathbf{0}, \tag{40}$$

where

$$P_{\max} = \begin{cases} 2 \times 10^3 \text{ Pa}, & t \leq 5 \text{ ms}, \\ 0, & t > 5 \text{ ms}. \end{cases}$$

The tube length is 3.3 cm, and the stent is located between $x_L = 0.825$ cm and $x_R = 2.475$ cm. The tube reference radius is $R = 1.5$ mm. The stent geometry is shown in Fig. 8. The values of all the parameters in the structure model are given in Table 1. The shell is clamped at the inlet and outlet. The pressure pulse propagates from left to right and it hits the right end of the tube at $t = 12$ ms. We show the results of our simulations for $t \in (0, 12)$ ms at six different snapshots. Figure 3 shows a sequence of 3D plots of structure displacement with blue denoting zero displacement, and red denoting maximal displacement of 2.6×10^{-6} m, which is around 0.2% of the reference cylinder radius. One can see that

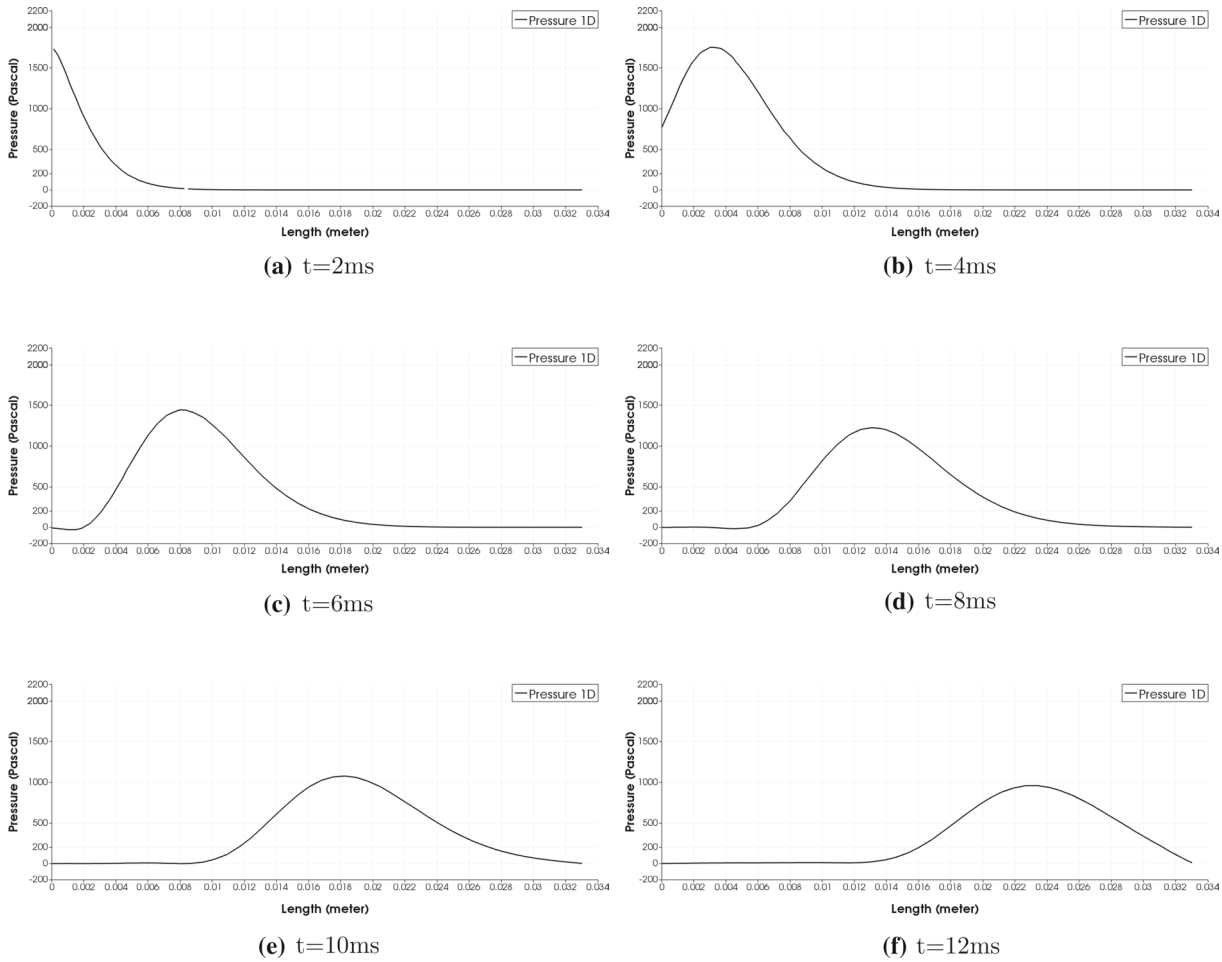

FIG. 4. 1D stent FSI simulations: the pressure along the line $y = 0, z = 0$ at six different times ($t = 2$ ms, 4 ms, 6 ms, 8 ms, 10 ms and 12 ms)

the incident wave traveling from left to right hits the left (proximal) end of the stent at $t \in (2, 3)$ ms, generating a reflected and a transmitted wave. The reflected wave travels backward and hits the left end of the tube which is clamped, generating another reflected wave traveling from left to right. The snapshot at $t = 4$ ms shows a superposition of the reflected waves. The blue dip corresponds to the wave reflected off the proximal end of the stent, while the red peaks correspond to the waves reflected off the left end of the tube. This can be seen better in the 2D plots of displacement, shown in Fig. 5. The transmitted wave continues to travel downstream the tube, giving rise to displacement in both the stent and the shell, which can be seen in the 3D and 1D plots, shown in Figs. 3 and 5. The 3D plots show the outline of the stent struts as the struts do not displace much, while the shell in between the struts has larger displacement. The shell displacement in between the struts is visible in Fig. 5 for $t \geq 4$ ms. The overall stiffness of the stent keeps the radial displacement in the stented region smaller than in the nonstented region, giving rise to a slight dampening of the pressure wave, see Fig. 4, as the velocity there increases. The axial and radial components of velocity are shown in Fig. 6. The snapshots at $t = 8$ ms are shown. This is the moment when the pressure wave enters the stented region of the tube. In the plot of the radial velocity, the red color denotes positive and the blue color negative radial displacement. The top half and

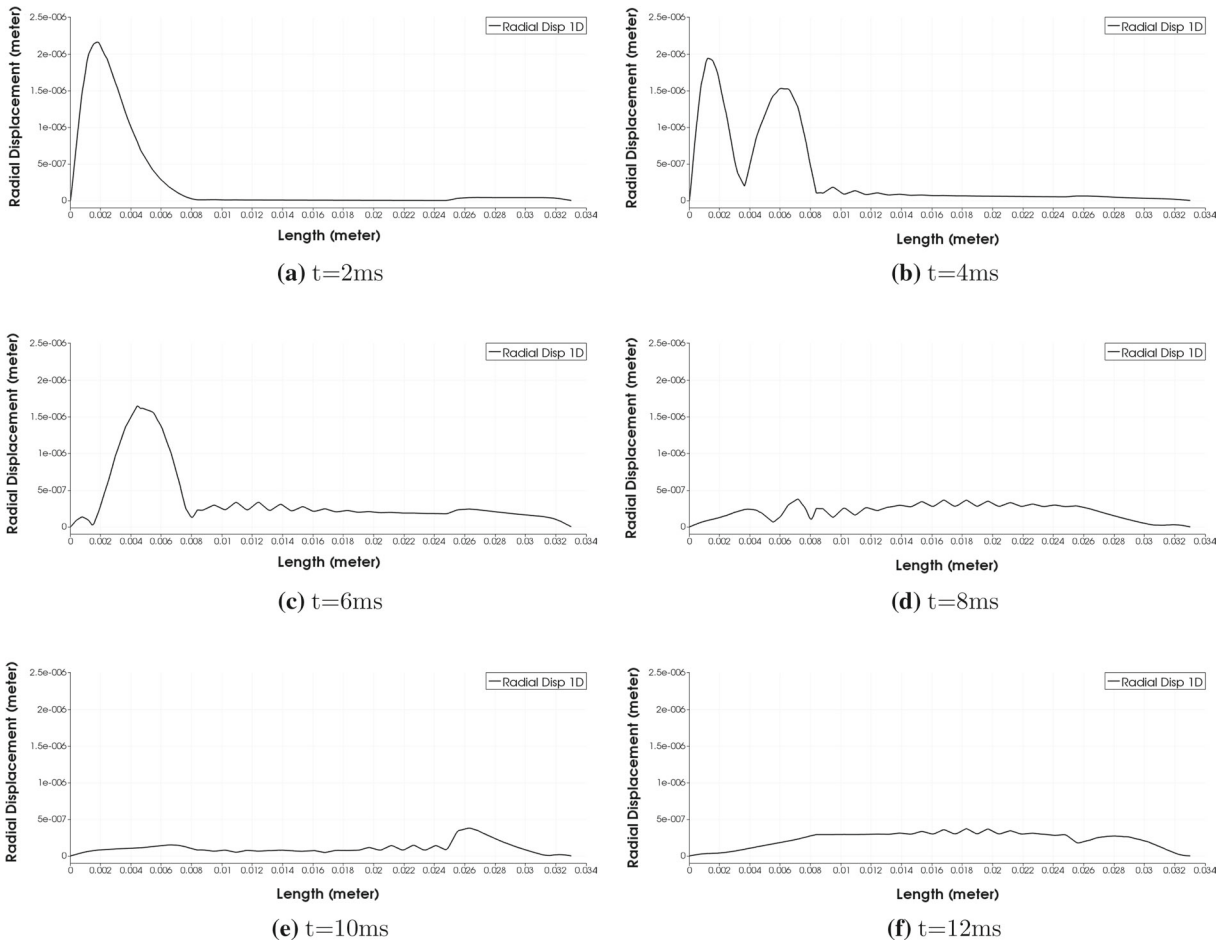

FIG. 5. 1D stent FSI simulations: radial displacement along the line $y = 0.015, z = 0$ at six different times ($t = 2$ ms, 4 ms, 6 ms, 8 ms, 10 ms and 12 ms)

FIG. 6. 1D stent FSI simulations: axial and radial components of fluid velocity at $t = 8$ ms (longitudinal cut through the middle of the tube)

bottom half have opposite colors because they correspond to the positive and negative parts of the y-axis. The red color in the top half of the tube denotes upward radial displacement, and the blue color denotes downward radial displacement. One can see how the radial velocity within the stented region of the tube is smaller than the radial velocity outside the stented region.

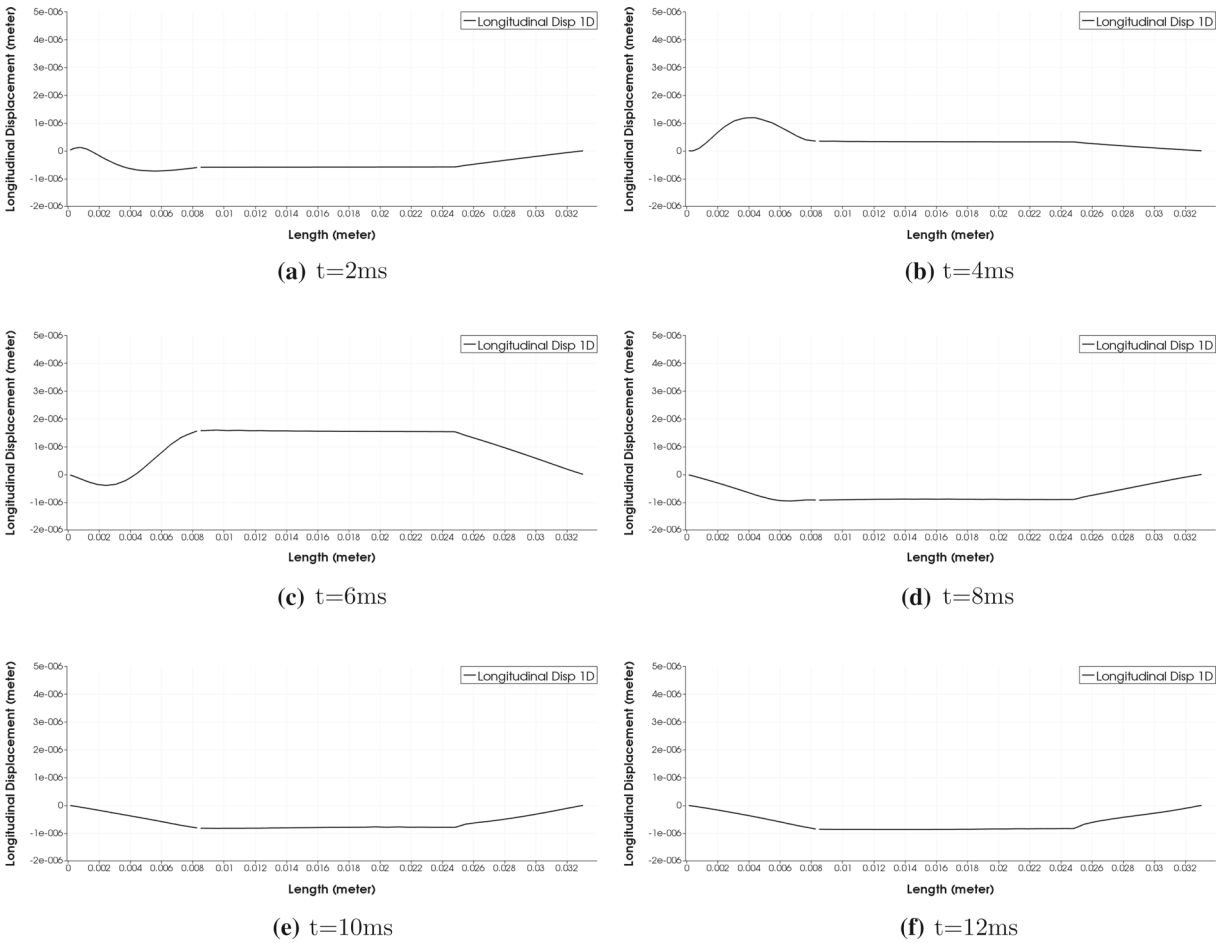

FIG. 7. 1D stent FSI simulations: longitudinal displacement along the line $y = 0.015, z = 0$ at six different times ($t = 2$ ms, 4 ms, 6 ms, 8 ms, 10 ms and 12 ms)

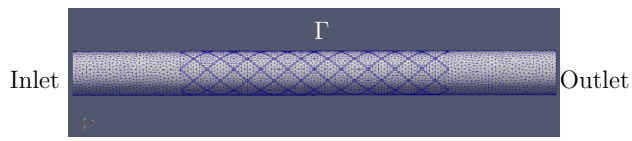

FIG. 8. 2D stent FSI: reference domain with an unstructured tetrahedron mesh

It is interesting to observe the behavior of longitudinal displacement, shown in Fig. 7. At the beginning when the pressure wave enters the tube and hits the proximal end of the stent, the longitudinal displacement becomes positive, see the plots for $t = 4$ ms and $t = 6$ ms. This means that the portion of the tube occupied by the stent behaves almost as a rigid body and causes a significant change in the total longitudinal displacement when the pressure wave hits the rigid part. Once the pressure wave is located well within the stented region, i.e., $t \geq 8$ ms, the longitudinal displacement of the tube becomes negative as the tube recoils from its longitudinal stretch.

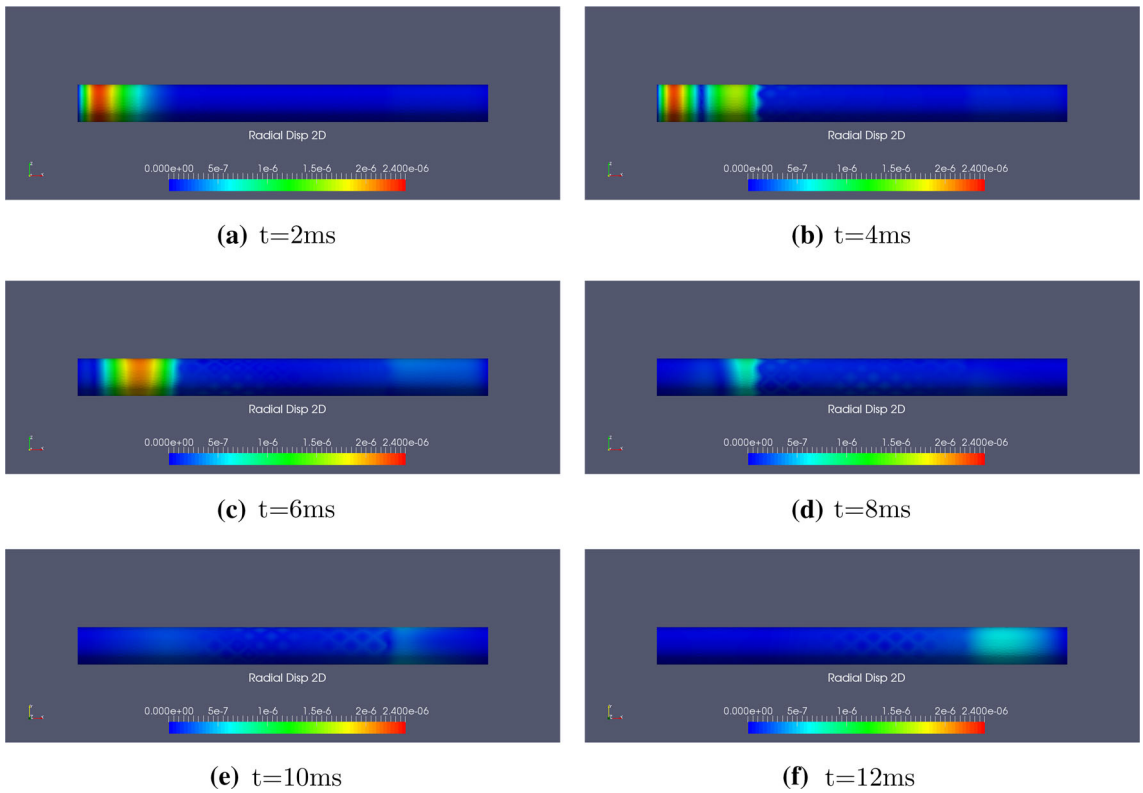

FIG. 9. 2D stent FSI simulation: the snapshots of radial displacement at six different times ($t = 2$ ms, 4 ms, 6 ms, 8 ms, 10 ms and 12 ms)

8.2. 2D stent FSI and comparison with 1D stent FSI

In this section, we present the FSI results in which the stent is considered to be a $2D$ body immersed in the Koiter shell and modeled by the change in the elasticity coefficients of the shell at the location of stent struts, as was done in [8]. We will be comparing the results of the FSI simulations obtained by modeling the stent as a 1D mesh, described above, with the stent modeled as a 2D structure, embedded in the shell. The first problem is referred to as 1D stent FSI, while the second one as 2D stent FSI. The boundary conditions, the location and geometry of the stent, and parameter values for the 2D stent FSI are the same as for the 1D stent FSI simulations. The computational domain is shown in Fig. 8. The resulting $3D$ plot of radial displacement is shown in Fig. 9, and the corresponding $1D$ plots of pressure, radial and longitudinal displacement are shown in Figs. 10, 11, and 12, respectively. The $1D$ plots of the $2D$ stent FSI simulations are superimposed over the plots of $1D$ stent model FSI simulations. Dashed lines denote results of the $2D$ stent model FSI simulations, while solid lines denote FSI simulations with the $1D$ stent model discussed in this paper.

One can see that the pressure wave propagation in both simulations are in very good agreement, as shown in Fig. 10. The radial and longitudinal displacements differ slightly, which is primarily due to the use of two different stent FSI models to study the corresponding FSI problem. It is interesting to notice that the radial displacement within the stented region is smaller for the $2D$ stent case, while the longitudinal displacement within the stented region is smaller for the $1D$ stent case for $t \leq 6$ ms.

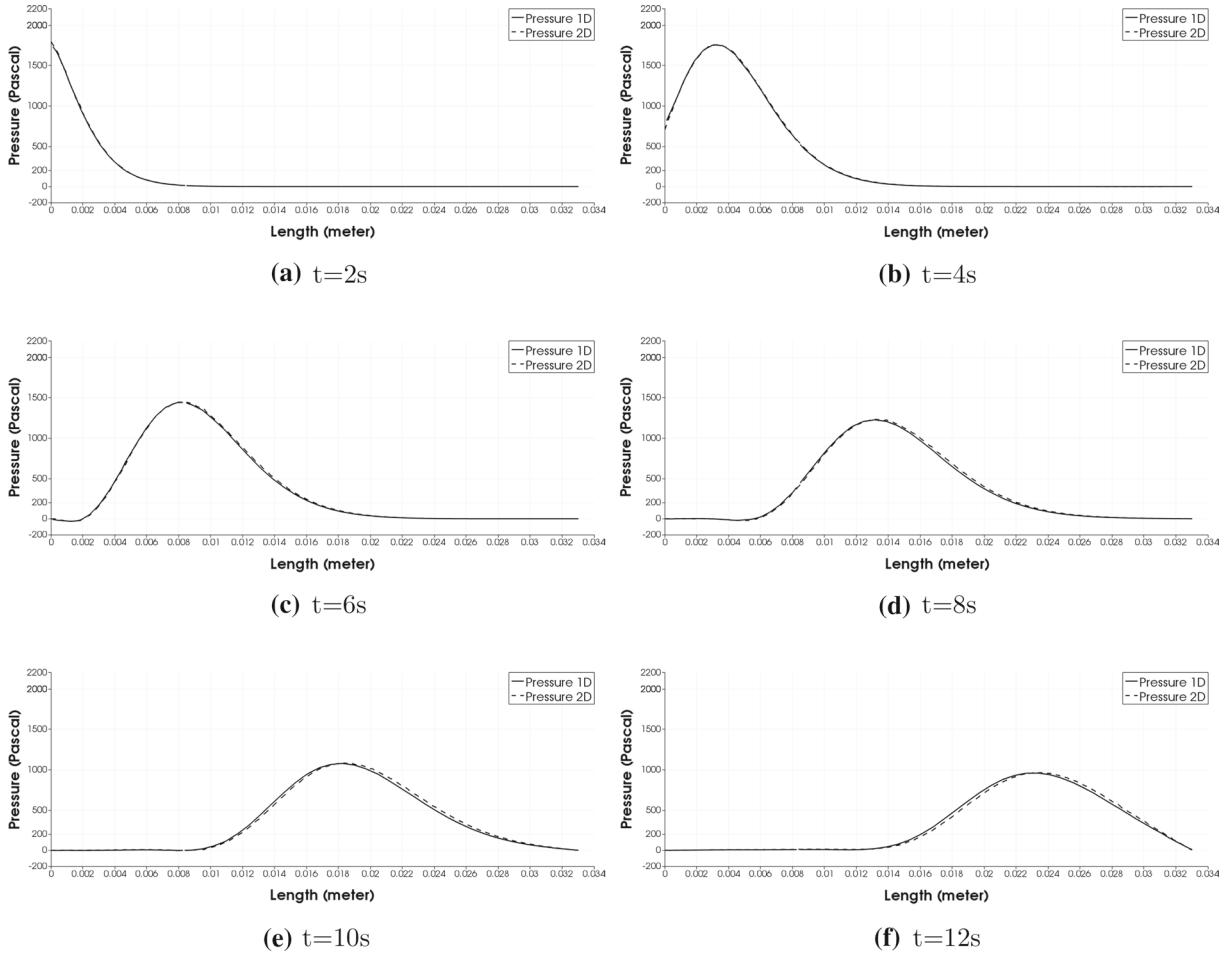

FIG. 10. The pressure along the line of $Y = 0, Z = 0$ at six different time moments ($t = 2$ s, 4 s, 6 s, 8 s, 10 s and 12 s)

There is a significantly smaller recoil in the longitudinal direction for the $2D$ stent case occurring for $t > 6$ ms. One explanation for this behavior is the inextensibility of the stent struts in the $1D$ model, which causes the $1D$ stent to behave almost like a rigid body in terms of longitudinal displacement. Most of the elastic energy of the $1D$ stent is spent on the deformation leading to the radial stent expansion.

It is important to notice that the assumptions of inextensibility and unshearability of rods in the $1D$ stent model were shown in [13] to be reasonable in the sense that static loading of the 1D stent produced results that are "consistent" with the observed full $3D$ stent behavior. More precisely, the work in [13] compared the 1D stent model deformation with the deformation produced by using full $3D$ elasticity to model the elastic behavior of stents. It was shown that under uniform inflation the L^∞-difference between the two models in the magnitude of displacement was $< 3\%$.

Therefore, we conclude that the FSI simulations obtained using the $1D$ stent model, coupled to the elastodynamics of the shell and the flow of an incompressible, viscous fluid produce reasonable results in the sense that they are close to the FSI simulations obtained by approximating the stent as a $2D$ body immersed in a $2D$ shell interacting with the flow of an incompressible, viscous fluid. The slight differences between the two models in the radial and longitudinal displacement can be attributed to the

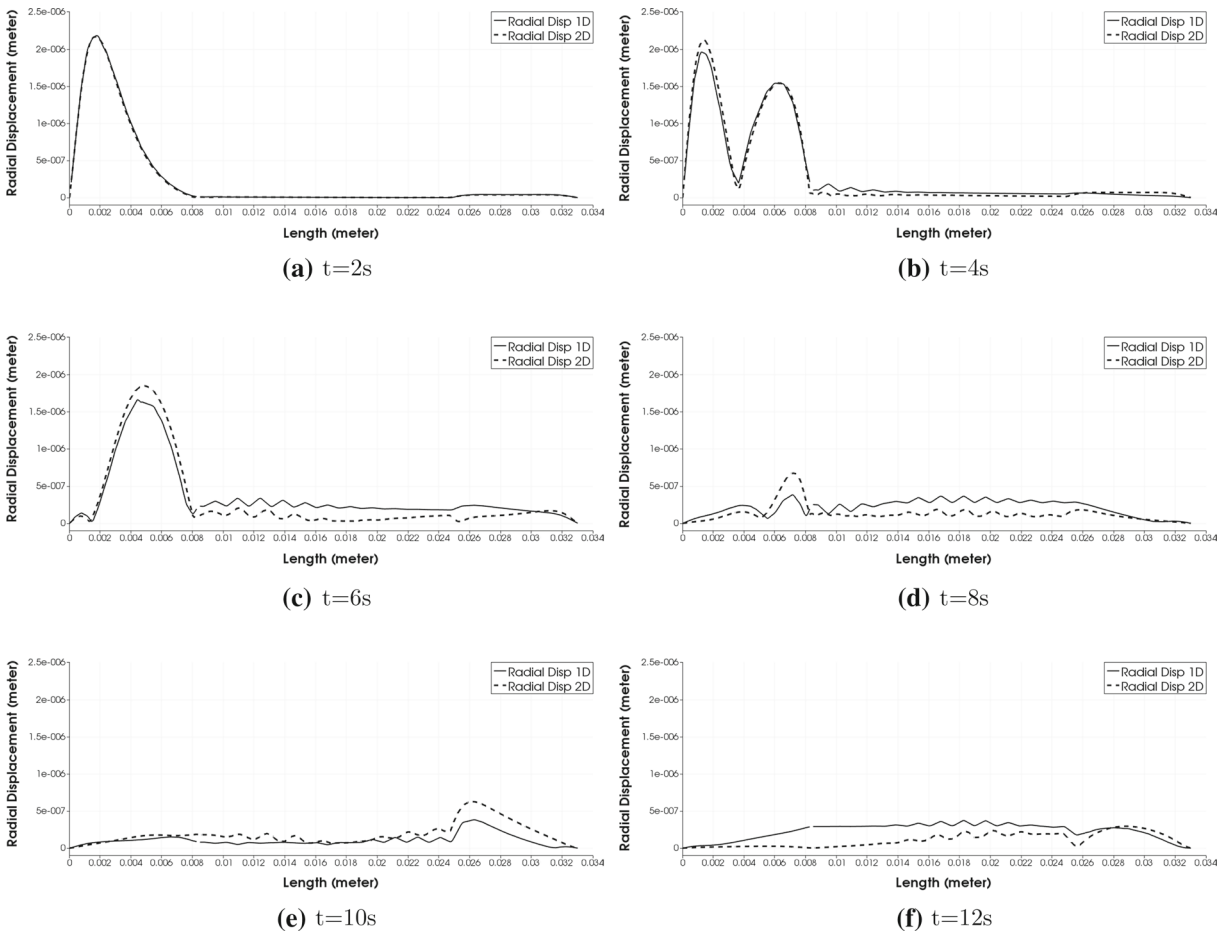

FIG. 11. The radial displacement along the line of $Y = 0.015, Z = 0$ at six different time moments ($t = 2$ s, 4 s, 6 s, 8 s, 10 s and 12 s)

difference in how the stent is modeled and coupled to the shell and fluid models. Considering the $1D$ stent model has the advantages of accounting for the physics of the stent–shell coupling, and can be extended to more complicated scenarios involving stent "dislodgement" and sliding, observed in certain patients treated with stents (which can be modeled by using a slip condition in the stent–shell coupling), and incomplete stent contact with the surrounding tissue (which gives rise to a free-boundary problem in the contact region between the stent and shell). Furthermore, computationally, simulating the thin stent struts in the 2D stent FSI model requires very fine 2D meshes at the location of stent struts to achieve reasonable accuracy. This is associated with large memory requirements and expensive computations. It was shown in [13] that 3D simulation of stents was converging to 1D results with the 3D mesh refinement, until memory limitation was reached beyond which 3D simulations were no longer possible. Similar conclusions hold for the comparison between 2D stent FSI and 1D stent FSI problems. Due to the issues associated with fine meshes at the location of stent struts in 2D stent FSi simulations, the computational cost and efficiency of 1D stent FSI simulations are significantly better when compared to 2D stent FSI simulations.

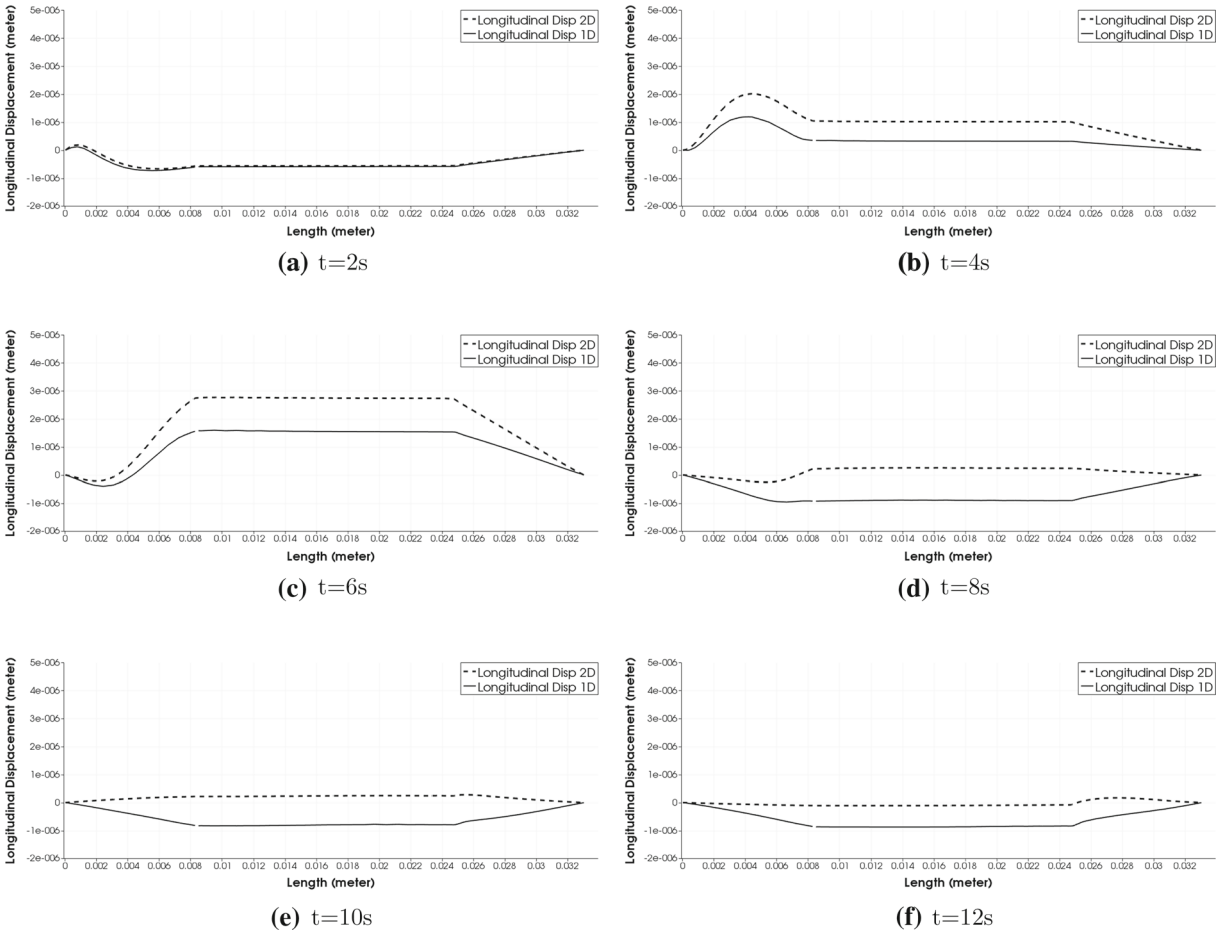

FIG. 12. The snapshots of the longitudinal displacement along the line of $Y = 0.015, Z = 0$ at six different time moments ($t = 2$ s, 4 s, 6 s, 8 s, 10 s and 12 s)

Acknowledgements

The work of S. Čanić was supported in part by the US National Science Foundation under Grants DMS-1613757, DMS-1318763, and by DMS-1311709. The work of M. Galić and B. Muha was supported in part by the Croatia-USA bilateral grant "Fluid-elastic structure interaction with the Navier slip boundary condition" associated with NSF DMS-1613757, and by the Croatian Science Foundation (Hrvatska Zaklada za Znanost) Grant Nos. 9477 and IP-2018-01-3706. The work of J. Tambača was supported by the Croatian Science Foundation Grant No. 9477.

9. Appendix (Notation)

The fluid

Constants	$\Omega = (0, L) \times B(0, R)$	Fluid domain
	μ_F	Dynamic viscosity
	ρ_F	Fluid density
Unknowns	$\mathbf{u}$	Velocity
	p	Pressure
	$\boldsymbol{v}$	Associated test functions

The shell

Constants	$\omega = (0, L) \times (0, 2\pi)$	Shell domain
	$\Gamma = \boldsymbol{\varphi}(\omega)$	Cylinder in $\mathbb{R}^3$
	h	Thickness
	L	Length
	R	Reference radius
	ρ_K	Shell density
Unknowns	$\boldsymbol{\eta}$	Displacement
	$\boldsymbol{v} = \partial_t \boldsymbol{\eta}$	Velocity of the displacement
	$\boldsymbol{\psi}$	Associated test functions

The mesh

Constants	$\omega_S = \bigcup_{i=1}^{n_E} \boldsymbol{\pi}_i(0, l_i)$	Mesh configuration on the shell
	A	Area of the cross section
	M	Moment of inertia
	H	Matrix of elastic properties
	Q	Local basis at each point
	ρ_S	Mesh density
Unknowns	$\mathbf{d}$	Displacement of the middle line
	$\mathbf{k} = \partial_t \mathbf{d}$	Velocity of the displacement
	$\boldsymbol{\xi}$	Associated test functions
	$\mathbf{w}$	Infinitesimal rotation of the cross section
	$\mathbf{z} = \partial_t \mathbf{w}$	Velocity of the rotation
	$\boldsymbol{\zeta}$	Associated test functions
	$\mathbf{q}, \mathbf{p}$	Contact moment and force

References

[1] Antman, S.S.: Nonlinear Problems of Elasticity. Applied Mathematical Sciences, vol. 107, 2nd edn. Springer, New York (2005)

[2] Avalos, G., Lasiecka, I., Triggiani, R.: Higher regularity of a coupled parabolic-hyperbolic fluid-structure interactive system. Georgian Math. J. **15**(3), 403–437 (2008)

[3] Avalos, G., Triggiani, R.: Semigroup well-posedness in the energy space of a parabolic–hyperbolic coupled Stokes–Lamé PDE system of fluid–structure interaction. Discrete Contin. Dyn. Syst. S **2**(3), 417–447 (2009)

[4] Badia, S., Quaini, A., Quarteroni, A.: Modular vs. non-modular preconditioners for fluid–structure systems with large added-mass effect. Comput. Methods Appl. Mech. Eng. **197**(49–50), 4216–4232 (2008)

[5] Bodnár, T., Galdi, G.P., Nečasová, Š. (eds.): Fluid–Structure Interaction and Biomedical Applications. Birkhäuser, Basel (2014)
[6] Bukac, M., Canic, S., Glowinski, R., Tambaca, J., Quaini, A.: Fluid-structure interaction in blood flow capturing non-zero longitudinal structure displacement. J. Comput. Phys. **235**, 515–541 (2013)
[7] Bukac, M., Canic, S., Muha, B.: A partitioned scheme for fluid–composite structure interaction problems. J. Comput. Phys. **281**, 493–517 (2015)
[8] Bukač, M., Čanić, S., Muha, B.: A nonlinear fluid–structure interaction problem in compliant arteries treated with vascular stents. Appl. Math. Optim. **73**(3), 433–473 (2016)
[9] Bukač, M., Muha, B.: Stability and convergence analysis of the extensions of the kinematically coupled scheme for the fluid–structure interaction. SIAM J. Numer. Anal. **54**(5), 3032–3061 (2016)
[10] Bukač, M., Čanić, S., Glowinski, R., Muha, B., Quaini, A.: A modular, operator-splitting scheme for fluid–structure interaction problems with thick structures. Int. J. Numer. Methods Fluids **74**(8), 577–604 (2014)
[11] Butany, J., Carmichael, K., Leong, S.W., Collins, M.J.: Coronary artery stents: identification and evaluation. J. Clin. Pathol. **58**(8), 795–804 (2005)
[12] Čanić, S., Galović, M., Ljulj, M., Tambača, J.: A dimension-reduction based coupled model of mesh-reinforced shells. SIAM J. Appl. Math. **77**(2), 744–769 (2017)
[13] Čanić, S., Tambača, J.: Cardiovascular stents as PDE nets: 1D vs. 3D. IMA J. Appl. Math. **77**(6), 748–770 (2012)
[14] Cesmelioglu, A.: Analysis of the coupled Navier–Stokes/Biot problem. J. Math. Anal. Appl. **456**(2), 970–991 (2017)
[15] Chacón Rebollo, T., Girault, V., Murat, F., Pironneau, O.: Analysis of a coupled fluid–structure model with applications to hemodynamics. SIAM J. Numer. Anal. **54**(2), 994–1019 (2016)
[16] Chambolle, A., Desjardins, B., Esteban, M.J., Grandmont, C.: Existence of weak solutions for the unsteady interaction of a viscous fluid with an elastic plate. J. Math. Fluid Mech. **7**(3), 368–404 (2005)
[17] Chueshov, I., Fastovska, T.: On interaction of circular cylindrical shells with a poiseuille type flow. Evolut. Equ. Control Theory **5**(4), 605–629 (2016)
[18] Chueshov, I., Ryzhkova, I.: Well-posedness and long time behavior for a class of fluid–plate interaction models. In: IFIP Conference on System Modeling and Optimization, pp. 328–337. Springer (2011)
[19] Chueshov, I., Ryzhkova, I.: On the interaction of an elasticwall with a Poiseuille-type flow. Ukr. Math. J. **65**(1), 158–177 (2013)
[20] Ciarlet, P.G.: Mathematical Elasticity. Volume I: Three-Dimensional Elasticity. Studies in Mathematics and Its Applications, vol. 20. North-Holland Publishing Co., Amsterdam (1988)
[21] Ciarlet, P.G.: Mathematical Elasticity. Volume III: Theory of Shells. Studies in Mathematics and Its Applications, vol. 29. North-Holland Publishing Co., Amsterdam (2000)
[22] Ciarlet, P.G., Lods, V.: Asymptotic analysis of linearly elastic shells. III. Justification of Koiter's shell equations. Arch. Ration. Mech. Anal. **136**(2), 191–200 (1996)
[23] Conca, C., Murat, F., Pironneau, O.: The Stokes and Navier–Stokes equations with boundary conditions involving the pressure. Jpn. J. Math. (N.S.) **20**(2), 279–318 (1994)
[24] Coutand, D., Shkoller, S.: The interaction between quasilinear elastodynamics and the Navier–Stokes equations. Arch. Ration. Mech. Anal. **179**(3), 303–352 (2006)
[25] Desjardins, B., Esteban, M.J.: Existence of weak solutions for the motion of rigid bodies in a viscous fluid. Arch. Ration. Mech. Anal. **146**(1), 59–71 (1999)
[26] Du, Q., Gunzburger, M.D., Hou, L.S., Lee, J.: Analysis of a linear fluid–structure interaction problem. Discrete Contin. Dyn. Syst. **9**(3), 633–650 (2003)
[27] Fernández, M.A.: Incremental displacement-correction schemes for incompressible fluid-structure interaction. Numer. Math. **123**(1), 21–65 (2013)
[28] Formaggia, L., Gerbeau, J.F., Nobile, F., Quarteroni, A.: On the coupling of 3D and 1D Navier–Stokes equations for flow problems in compliant vessels. Comput. Methods Appl. Mech. Eng. **191**(6–7), 561–582 (2001)
[29] Galdi, G.P.: On the motion of a rigid body in a viscous liquid: a mathematical analysis with applications. In: Handbook of Mathematical Fluid Synamics, vol. I, pp. 653–791. North-Holland, Amsterdam (2002)
[30] Glowinski, R.: Finite element methods for incompressible viscous flow. In: Handbook of Numerical Analysis, vol. IX, pp. 3–1176. North-Holland, Amsterdam (2003)
[31] Glowinski, R., Osher, S.J. (eds.): Splitting Methods in Communication, Imaging, Science, and Engineering. Scientific Computation. Springer, Cham (2016)
[32] Grandmont, C., Hillairet, M.: Existence of global strong solutions to a beam–fluid interaction system. Arch. Ration. Mech. Anal. **220**(3), 1283–1333 (2016)
[33] Griso, G.: Asymptotic behavior of structures made of curved rods. Anal. Appl. (Singap.) **6**(1), 11–22 (2008)
[34] Grubisic, L., Tambaca, J.: Direct solution method for the equilibrium problem for elastic stents. Numer. Linear Algebra Appl. **(accepted)**. https://doi.org/10.1002/nla.2231
[35] Grubišić, L., Iveković, J., Tambača, J., Žugec, B.: Mixed formulation of the one-dimensional equilibrium model for elastic stents. Rad Hrvatske akademije znanosti i umjetnosti: Matematičke znanosti **532**(21), 219–240 (2017)

[36] Guidoboni, G., Glowinski, R., Cavallini, N., Čanić, S.: Stable loosely-coupled-type algorithm for fluid–structure interaction in blood flow. J. Comput. Phys. **228**(18), 6916–6937 (2009)
[37] Hou, G., Wang, J., Layton, A.: Numerical methods for fluid-structure interaction—a review. Commun. Comput. Phys. **12**(2), 337–377 (2012)
[38] Ignatova, M., Kukavica, I., Lasiecka, I., Tuffaha, A.: On well-posedness and small data global existence for an interface damped free boundary fluid–structure model. Nonlinearity **27**(3), 467–499 (2014)
[39] Jurak, M., Tambača, J.: Derivation and justification of a curved rod model. Math. Models Methods Appl. Sci. **9**(7), 991–1014 (1999)
[40] Jurak, M., Tambača, J.: Linear curved rod model: general curve. Math. Models Methods Appl. Sci. **11**(7), 1237–1252 (2001)
[41] Koiter, W.T.: On the foundations of the linear theory of thin elastic shells. I. Nederl. Akad. Wetensch. Proc. Ser. B. **73**, 169–182 (1970)
[42] Koiter, W.T.: On the foundations of the linear theory of thin elastic shells. II. Nederl. Akad. Wetensch. Proc. Ser. B **73**, 183–195 (1970)
[43] Kukavica, I., Tuffaha, A., Ziane, M.: Strong solutions to a Navier–Stokes–Lamé system on a domain with a non-flat boundary. Nonlinearity **24**(1), 159–176 (2011)
[44] Lengeler, D., Růžička, M.: Weak solutions for an incompressible Newtonian fluid interacting with a Koiter type shell. Arch. Ration. Mech. Anal. **211**(1), 205–255 (2014)
[45] Lions, J.-L.: Quelques méthodes de résolution des problèmes aux limites non linéaires. Gauthier-Villars, Paris (1969)
[46] Lukáčová-Medvid'ová, M., Rusnáková, G., Hundertmark-Zaušková, A.: Kinematic splitting algorithm for fluid–structure interaction in hemodynamics. Comput. Methods Appl. Mech. Eng. **265**, 83–106 (2013)
[47] Muha, B., Čanić, S.: Existence of a weak solution to a nonlinear fluid–structure interaction problem modeling the flow of an incompressible, viscous fluid in a cylinder with deformable walls. Arch. Ration. Mech. Anal. **207**(3), 919–968 (2013)
[48] Muha, B., Čanić, S.: A nonlinear, 3D fluid–structure interaction problem driven by the time-dependent dynamic pressure data: a constructive existence proof. Commun. Inf. Syst. **13**(3), 357–397 (2013)
[49] Muha, B., Čanić, S.: Existence of a solution to a fluid–multi-layered-structure interaction problem. J. Differ. Equ. **256**(2), 658–706 (2014)
[50] Muha, B., Čanić, S.: Fluid-structure interaction between an incompressible, viscous 3D fluid and an elastic shell with nonlinear Koiter membrane energy. Interfaces Free Bound. **17**(4), 465–495 (2015)
[51] Muha, B., Čanić, S.: Existence of a weak solution to a fluid–elastic structure interaction problem with the Navier slip boundary condition. J. Differ. Equ. **260**(12), 8550–8589 (2016)
[52] Tambača, J., Kosor, M., Čanić, S., Paniagua, D.: Mathematical modeling of vascular stents. SIAM J. Appl. Math. **70**(6), 1922–1952 (2010)
[53] Tambača, J., Tutek, Z.: A new linear Naghdi type shell model for shells with little regularity. Appl. Math. Model. **40**(23–24), 10549–10562 (2016)

Sunčica Čanić
Department of Mathematics
University of Houston
Houston
USA
e-mail: canics@berkeley.edu

Sunčica Čanić and Yifan Wang
UC Berkeley
Berkeley
USA

Marija Galić, Matko Ljulj, Boris Muha and Josip Tambača
Department of Mathematics, Faculty of Science
University of Zagreb
Zagreb
Croatia

(Received: February 17, 2018; revised: January 23, 2019)